



Records of geomagnetism, climate, and tectonics across a Paleoproterozoic erosion surface



Kyle Bradley^{a,*}, Benjamin P. Weiss^a, Roger Buick^b

^a Department of Earth, Atmospheric, and Planetary Sciences, Massachusetts Institute of Technology, Cambridge, MA, USA

^b Department of Earth and Space Sciences and Astrobiology Program, University of Washington, Seattle, WA, USA

ARTICLE INFO

Article history:

Received 22 August 2014

Received in revised form 23 February 2015

Accepted 5 March 2015

Available online xxxx

Editor: T. Elliott

Keywords:

Archean

paleomagnetism

geomagnetism

Pilbara

Kaapvaal

Vaalbara

ABSTRACT

Paleomagnetism has provided key constraints on the evolution of Earth's climate, geomagnetic field, and continental geography through Phanerozoic and Proterozoic time. Extending these constraints into the Archean eon has been particularly challenging due to the paucity of the ancient rock record. Here we report paleomagnetic measurements on the NASA Astrobiology Drilling Project (ABDP)-8 core drilled through one of the world's least deformed and least metamorphosed Paleoproterozoic [3200–3600 million year old (Ma)] rock successions located in the East Strelley Belt of the eastern Pilbara Craton, Australia. Our results show that the ~3350 Ma Euro Basalt preserves a shallow magnetic inclination that appears to have formed as a result of early seafloor hydrothermal alteration, suggesting that the evaporitic carbonate platform of the conformably underlying Strelley Pool Formation was deposited in a near-equatorial location. This is consistent with (although does not require) late Paleoproterozoic climatic zoning, low orbital obliquity, and a geocentric axial dipole (GAD) field geometry similar to that of the Phanerozoic. The Euro Basalt paleopole overlaps with previously published Paleoproterozoic poles from the East Pilbara craton and with time-equivalent poles reported from the Barberton Greenstone Belt of the Kaapvaal craton, supporting the existence of a Paleoproterozoic Vaalbara continental aggregation.

© 2015 Elsevier B.V. All rights reserved.

1. Introduction

Planetary orbital obliquity determines the distribution of insolation over Earth's surface. Modern Earth has a low obliquity (23°) that controls the Hadley cell circulation pattern, leading to moisture-rich tropics and carbonate platforms equatorwards of ~30° latitude (Salby, 1996). Early paleomagnetic studies observed that carbonate platforms were deposited below ~30° paleolatitude throughout much of the Phanerozoic era if a geocentric axial dipole (GAD) field geometry is assumed (Briden, 1970). This consistency helped establish the GAD hypothesis as a foundational principle in paleomagnetism for characterizing polar wander, continental reconstructions, and the unusual paleolatitudes of climate-sensitive rocks like glacial sediments associated with the hypothesized "Snowball Earth" events (Evans, 2006).

While Earth's geomagnetic field existed as early as ~3450 Ma (Biggin et al., 2011; Tarduno et al., 2007, 2010; Usui et al., 2009), reconstruction of the earliest field geometry using globally-

distributed paleomagnetic data is not feasible due severe under-sampling of Paleoproterozoic rocks. Furthermore, the climate pattern at this time would have depended on many unconstrained factors, including the configuration and proportion of land masses and oceans, the intensity of insolation, the planetary obliquity, and the temperature and composition of the atmosphere and ocean (Spiegel et al., 2009). Hence, there is little prospect of fully characterizing Earth's earliest climate zonation using traditional paleomagnetic methods. Nevertheless, the magnetization of very rare, well-preserved Paleoproterozoic volcanic rocks interbedded with chemical sediments can be used to test whether the basic conditions that have prevailed since ~2000 Ma, including a GAD field geometry, obliquity <54°, and a latitudinally zoned climate (Evans, 2006), might have originated in much deeper time.

If the GAD hypothesis is assumed to hold for Paleoproterozoic time, then paleomagnetic data from this era can also be used to infer relative positions of some of the earliest known continental masses. In particular, they could be used to test the hypothesis that the Kaapvaal craton of South Africa and the East Pilbara craton of Western Australia are the partial remnants of a single Archean proto-continental mass, termed Vaalbara (Cheney et al., 1988). Such an association has long been suggested by the broad similarity between their Neoproterozoic supracrustal successions and associated intrusive suites. The earliest paleomagnetic tests of the

* Corresponding author.

E-mail address: kbradley@ntu.edu.sg (K. Bradley).

¹ Now at the Earth Observatory of Singapore, Nanyang Technological University, Singapore 639798.

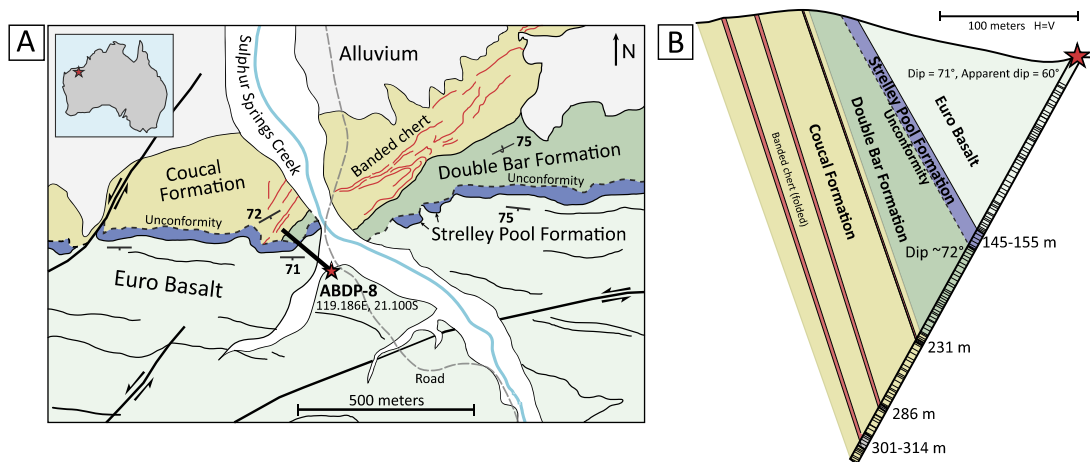


Fig. 1. Geological setting. (A) Generalized geological map of the study area (after Van Kranendonk (2000) and interpretation of satellite imagery). Star: ABDP-8 drill site located at 21.1000°S, 119.1864°E. Faults (bold arrows) and strikes and dips of bedding (bars with tick marks and dip angles) shown in selected locations. (B) Geometry of the ABDP-8 drill core and rock units at depth, with each of our subsamples indicated by a black band. C1, C2, and C3 are banded chert horizons mapped within the uppermost Coucal Formation to the northeast of the drill site.

Vaalbara hypothesis had to rely on comparisons of inferred paleolatitude alone (Zegers et al., 1998), but publication of more reliable Neoproterozoic paleomagnetic poles from both terranes has made a direct plate-tectonic restoration more feasible (de Kock et al., 2009 and references therein). Furthermore, selected ~3450 Ma Paleoproterozoic poles were considered by Biggin et al. (2011) to be consistent, broadly, with either the Zegers et al. (1998) or de Kock et al. (2009) Vaalbara reconstruction models, under alternative assignments of geomagnetic polarity for those poles. While the paleomagnetic record from the Kaapvaal Paleoproterozoic has improved markedly in recent years (Biggin et al., 2011), the time-equivalent dataset from the East Pilbara craton remains small and relatively unreliable.

Remanent magnetization in well-preserved rocks from the East Pilbara craton therefore has great potential for directly testing multiple hypotheses of uniformitarian conditions in Paleoproterozoic time. With these goals in mind, we examined the ABDP-8 core drilled near Sulphur Springs Creek in Western Australia (Fig. 1A). The ABDP-8 core has two major advantages over outcrop samples: 1) it is unaffected by the modern oxidative weathering and lightning strikes that have largely remagnetized surface exposures of low grade Paleoproterozoic rocks (e.g., Strik et al., 2003; Carporzen et al., 2012), and 2) it provides a semi-continuous stratigraphic time sequence through two of the oldest known but minimally metamorphosed rock sequences in the world.

The East Strelley Belt contains the only exposures of the Coonterunah Subgroup of the Warrawoona Group, the oldest known supracrustal rocks in Australia (Buick et al., 1995). The base of the Coonterunah Subgroup consists of the undated tholeiitic basalts and komatiites of the Table Top Formation, which grade upward into 3515 ± 3 Ma rhyolites, dacites and andesites of the Coucal Formation (Buick et al., 1995; Green et al., 2000). Thin, banded cherts that occur near the top of the Coucal Formation are silicified ashes that can be traced for several kilometers (Smithies et al., 2007). The Coucal Formation is overlain by tholeiitic basalts of the Double Bar Formation; a felsic volcanic near the top of this formation has a reported age of 3498 ± 2 Ma (Nelson, 2002). The Coonterunah Subgroup was intruded by the ≥3468 ± 4 Ma Carlindie Granitoid Complex, causing greenschist facies metamorphism (amphibolite facies near the intrusive contact) accompanied by open folding (Buick et al., 1995) and development of a weak foliation (Blewett, 2002). Deformation after ~3426 Ma led to emergence and erosion of the upper Warrawoona Group section, producing a regional paleo-exposure surface (Buick et al., 1995), upon which

the >3350 Ma Strelley Pool Formation was deposited during a magmatic hiatus (Allwood et al., 2006; Hickman, 2008). The overlying Kelly Group consists of komatiites and tholeiitic pillow basalts of the 3350–3335 Ma Euro Basalt, which are conformably overlain by the 3325–3315 Ma felsic volcanics of the Wyman Formation and the Charteris Basalt (Thorpe et al., 1992). In the East Strelley Belt, an unconformity beneath sediments of the ca. 3190 ± 10 Ma Soanesville Group locally eroded the Kelly Group above the Euro Basalt as well as the entire Sulphur Springs Group. Southward shallowing of dips away from the Carlindie Granitoid Complex is evidence for progressive doming that commenced soon after emplacement of the Euro Basalt and continued through deposition of the De Grey Supergroup (Van Kranendonk, 2000). Bedding orientations within the East Strelley Belt were probably further modified during regional transpression on the neighboring Lalla Rookh – Western Shaw structural corridor at ~2940 Ma (Van Kranendonk and Collins, 1998) and during minor late Archean doming that cannot be constrained in age or precise geometry due to subsequent erosion of rocks younger than ~2.8 Ga.

The ABDP-8 core transects greenschist facies rocks of the Coucal Formation (120 m of stratigraphy) and Double Bar Formation (50 m of stratigraphy) (Fig. 1B), the angular unconformity and a thin sequence of sedimentary rocks of the Strelley Pool Formation (25 m of stratigraphy), and the Euro Basalt (140 m of stratigraphy). While rocks in the greater East Strelley Belt have experienced metamorphic grades of prehnite–pumpellyite to lowermost amphibolite facies (Green et al., 2000) at temperatures between ~250 and ~500 °C (Harnmeijer, 2009), at the ABDP-8 site the metamorphic grades are lower to mid-greenschist beneath the angular unconformity and prehnite–pumpellyite above.

2. Sampling and lithological characteristics

We acquired 185 samples at approximately equal intervals from the ABDP-8 quarter core housed at Arizona State University (ASU) using a 2.54 cm diameter diamond drill bit mounted on a drill press. The mineralogies of representative specimens were characterized using scanning electron microscopy and energy dispersive spectroscopy analyses on polished end chip surfaces using a JEOL JXA-733 Superprobe housed in the MIT Electron Microprobe Facility. Volcanic rocks of the Euro Basalt consist of the mineral assemblage albite–actinolite–epidote–pumpellyite with a variably developed propylitic overprint characterized by a chlorite, quartz, and carbonate minerals. Accessory minerals occur as

fine, dispersed grains and include chalcopryrite, leucoxene or rutile, chromite, titanite, and apatite. While primary igneous minerals have been invariably replaced by secondary assemblages, pillow rims and inter-pillow hyaloclastites and breccias are identifiable in core segments as well as in outcrop. Similar mineral assemblages and alteration patterns have been described from altered Paleoproterozoic subaqueous basalts in the North Pole Dome region (Kitajima et al., 2001), where they have been inferred to have resulted from low-temperature hydrothermal alteration in a seafloor environment. Samples from the Double Bar and Coucal Formations consist of the assemblage quartz–chlorite–calcite–phengite–leucoxene–pyrite–arsenopyrite, with apatite and xenotime as accessories. This assemblage reflects greenschist facies metamorphism driven by intrusion of the neighboring Carlindie granitoid complex, overprinted by a phyllic alteration that is more strongly developed near the contact with the Strelley Pool Formation.

As pyrrhotite is a common magnetic carrier in altered volcanic rocks, we quantitatively assessed the chemical composition of the iron sulfide minerals using energy dispersive spectroscopy on the JEOL JXA-733 operated at 15 kV and 10 mA, with a focused beam diameter of $\sim 1 \mu\text{m}$ and FeS_2 (pyrite) standards. All analyzed grains yielded an estimated $\text{Fe}/(\text{Fe} + \text{S})$ atomic ratio of $\sim 33 \pm 5\%$, consistent with stoichiometric pyrite and chalcopryrite. We observed abundant trellised leucoxene (TiO_2) structures within the Double Bar Formation specimens, which we interpret as remnants of igneous titanomagnetite grains exhibiting magnetite–ilmenite oxyexsolution textures (Fig. S1). Subsequent to the exsolution, the interlocked ilmenite and magnetite were dissolved, leaving behind pure titanium oxide in place of ilmenite, and chlorite + quartz in place of magnetite. Despite systematic element mapping, we did not identify iron oxide minerals in any samples, with the exception of fractured and fragmented chromite within the Euro Basalt and the Double Bar Formation. The magnetic minerals within the volcanic specimens are therefore all very fine-grained ($< 1 \mu\text{m}$ in diameter).

3. Rock magnetism

The ability of a rock to retain a faithful record of paleofield direction over long time intervals depends primarily on the composition, size distribution, and shape of the magnetic grains. The petrographic evidence for complete dissolution of primary magnetic minerals in the Double Bar Formation requires destruction of the greatest part or all of any original thermoremanent or thermochemical remanent magnetization during subsequent bulk alteration. The timing of this alteration and the remaining ability of these rocks to record ancient magnetic field directions is therefore of paramount importance to interpretation of their paleomagnetic signatures. We conducted a suite of rock magnetic experiments aimed at characterizing the magnetic mineralogy and, to a limited extent, the grain size distribution of the sampled units.

We subjected 10 end chips to progressive thermal demagnetization of composite isothermal remanent magnetization (IRM) (Lowrie, 1990). IRM components of 0.9, 0.5, and 0.12 T applied sequentially in three perpendicular directions were thermally demagnetized in order to determine the blocking temperature spectrum of different coercivity fractions (Fig. 2C, D). These data, as well as thermal unblocking spectra of NRM (Fig. 2A, B), indicate that all specimens are dominated by a low coercivity ($< 0.12 \text{ T}$) phase that unblocks between $530\text{--}550^\circ\text{C}$, consistent with low-Ti titanomagnetite. We observed additional unblocking between $565\text{--}580^\circ\text{C}$ in some specimens, suggesting the presence of stoichiometric magnetite. Unblocking of all three coercivity components between the 310°C and 350°C temperature steps may indicate the presence of either monoclinic pyrrhotite, titanomagnetite,

or titanomaghemite grains. The presence of visible sulfide grains in these samples strongly favors pyrrhotite over these other possibilities. Although the equivalent low unblocking temperature magnetizations could conceivably retain a record of the geomagnetic field direction in minerals that grew during early hydrothermal alteration or slightly later subaerial weathering, they could alternatively represent weathering or alteration driven grain-growth chemical remanent magnetizations lying generally parallel to and inherited from the dominant low-Ti titanomagnetite magnetization.

The dominant presence of magnetite admixed with another phase, probably pyrrhotite, is confirmed by our measurements of the forward S ratio (Kruiver and Passier, 2001) (IRM at 0.3 T/IRM at 0.9 T) on 65 end chips (Fig. 2D). S ratios near 1 indicate dominance of a low coercivity phase (such as magnetite), while S ratios < 0.95 indicate significant quantities of high-coercivity phases like hematite or pyrrhotite. Euro Basalt specimens yielded S ratios of 0.95–0.99 and Strelley Pool Formation specimens yielded S ratios of ~ 0.9 . We note that use of the forward S ratio in this way assumes non-interacting magnetic carriers; this was confirmed for our specimens by comparison of IRM acquisition and AF demagnetization curves which indicate Cisowski R-values (Cisowski, 1981) near 0.5.

To constrain the magnetic grain size, we subjected 10 representative end chips to a modified Lowrie–Fuller test (Dunlop et al., 1973; Johnson et al., 1975; Lowrie and Fuller, 1971; Xu and Dunlop, 1995). We first induced an anhysteretic remanent magnetization (ARM) using a peak ac field of 215 mT and a dc bias field from 0.2 to 2 mT in progressive 0.2 mT increments, which we then AF demagnetized in 4 mT increments up to 215 mT. We subsequently AF demagnetized a 215 mT IRM following the same protocol. Nine specimens yielded low field (L)-type behavior (ARM more resistant than IRM), and one produced a neutral result (Fig. 2E, F). The dominantly L-type results are consistent with the presence of a population of grains exhibiting single domain to pseudo single domain (PSD)-type behavior under AF demagnetization. Furthermore, we observe no difference in thermal demagnetization behavior between the Euro Basalt and Coonterunah Subgroup specimens.

This is consistent with our hysteresis measurements, which were conducted on 30 end chips using an ADE 1660 VSM in the laboratory of C. Ross at MIT (Fig. 3A, B). Combined with our measurements of the coercivity of remanence on the same specimens by the backfield method (Dunlop and Özdemir, 2001) using a 2G Enterprises Superconducting Rock Magnetometer (SRM) 755, these yielded hysteresis parameters for the Euro Basalt specimens falling within the PSD-superparamagnetic (SP) mixing field of the Day–Dunlop diagram (Fig. 3C). This is typical of most natural rocks preserving paleomagnetic remanences. Most Coonterunah Subgroup specimens exhibit weak saturation magnetizations and are dominated by a paramagnetic component that did not reach saturation under the maximum applied field, resulting in noisier hysteresis loops after subtraction of a linear paramagnetic trend estimated separately for each sample (Fig. 3B, inset). This phenomenon is particularly pronounced in samples from the sub-unconformity alteration zone. Interpretable loops measured from Coonterunah rocks are from the stratigraphically lowest, least altered part of the core (Fig. 3B). Like the Euro Basalt, these specimens fall in the PSD-SP mixing field on the Day diagram although with an overall slightly coarser inferred grain size. This slightly coarser inferred grain size is the only difference that we can discern between the magnetic mineralogies of the Euro Basalt and Coonterunah Subgroup volcanics. In general, both Subgroups have the same mineralogy and have a broad distribution of grains lying dominantly in the PSD-SP mixing field and are therefore both capable of preserving ancient magnetizations.

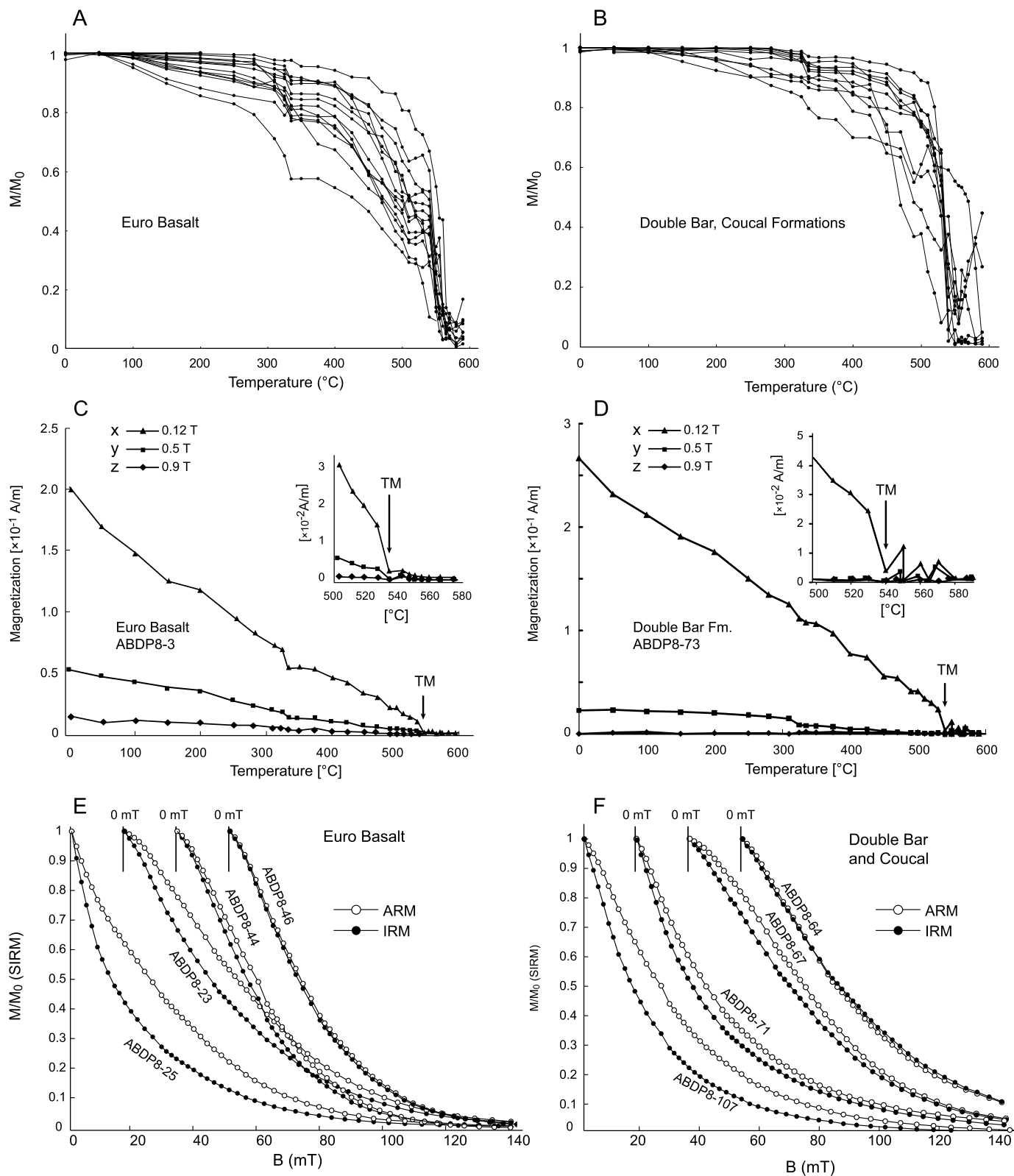


Fig. 2. Rock magnetic measurements. (A, B) Normalized unblocking spectra of NRM during progressive thermal demagnetization after AF demagnetization to 20 mT. (C, D) Representative results of progressive thermal demagnetization of orthogonal laboratory-induced IRMs (Lowrie, 1990) on Euro Basalt subsample ABDP8-3 (C) and Double Bar Formation subsample ABDP8-73 (D). Insets show demagnetization above 500°C with inferred Curie temperature of low-Ti titanomagnetite (TM) labeled. (E, F) Results of the modified Lowrie–Fuller test (Johnson et al., 1975) on Euro Basalt subsamples ABDP8-23, -25, -45, and -46 (E) and Double Bar Formation subsamples ABDP8-64, -67, -71, and -107 (F). Filled symbols show progressive AF demagnetization of an IRM and open symbols show progressive AF demagnetization of an ARM applied with a 215 mT peak AC field with a 2 mT DC bias field. Curves for individual samples are offset along the horizontal axis for clarity.

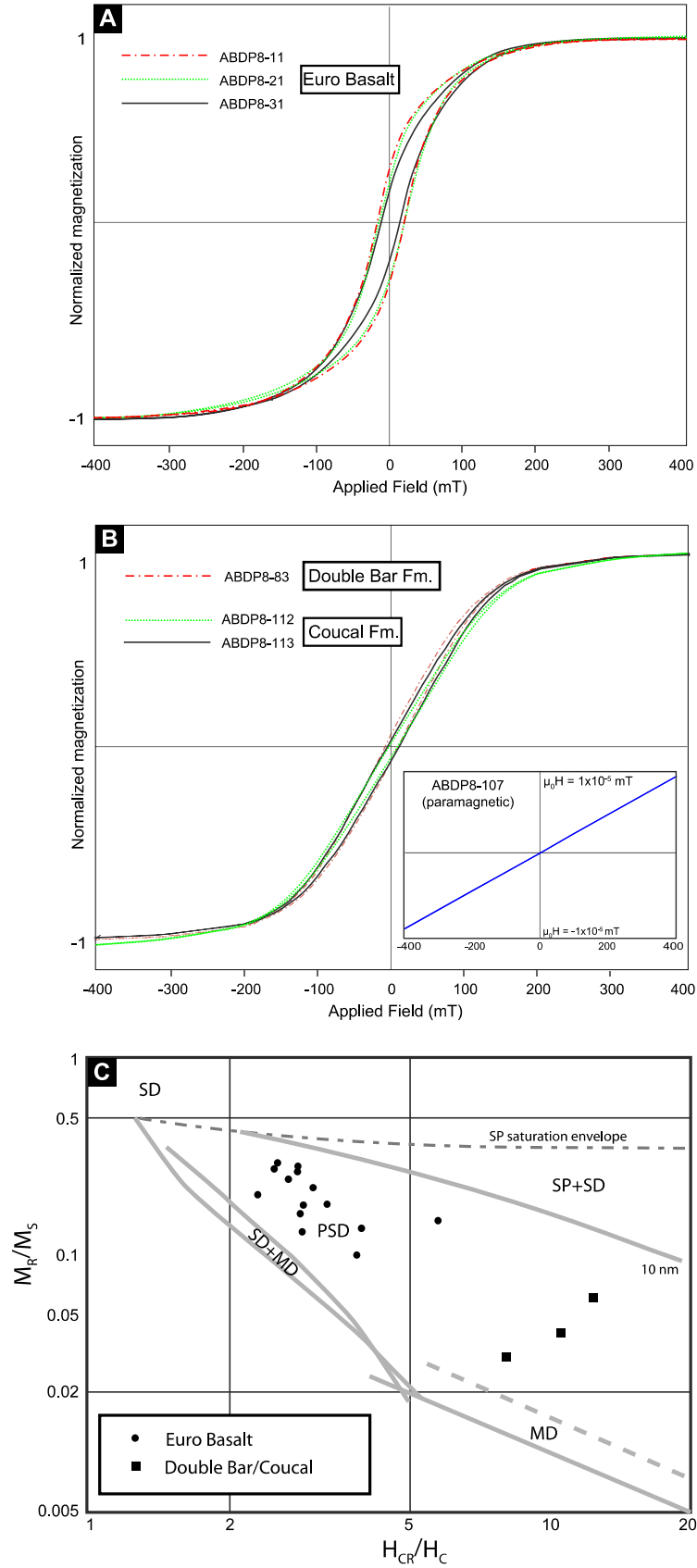


Fig. 3. Magnetic hysteresis. (A, B) Representative hysteresis loops for selected specimens after subtraction of a linear paramagnetic component for Euro Basalt subsamples ABDP8-11, -21, and -31 (A) and Double Bar and Coucal Formation subsamples ABDP8-83, -112, and -113 (B). Inset in (B) shows sample ABDP8-107 before paramagnetic component subtraction. (C) Day–Dunlop (Dunlop, 2002) diagram showing the ratio of coercivity of remanence to coercivity (H_{CR}/H_C) as a function of the ratio of saturation remanence to saturation magnetization (M_R/M_S) for all measured hysteresis loops. Lines shown are the SD-multidomain (MD) mixing line, the MD trend line, and the SP–SD mixing line (for 10 nm SP grains). Both the Euro Basalt and Coucal/Double Bar specimens (circles) fall within the PSD–SP mixing field.

Table 1

Fisher mean directions determined in this study. *N*: number of component fits; *Dg*: geographic declination; *Ig*: geographic inclination; *k*: Precision parameter of Fisher mean; α_{95} : angular radius of circle of 95% confidence; *R*: length of resultant of unit vectors *Ds*: declination corrected for bedding dip of Euro Basalt; *Is*: inclination corrected for bedding dip of Euro Basalt; *Dss*: declination corrected for remaining 36° of bedding dip after tilt correction of Euro Basalt; *Iss*: inclination corrected for remaining 36° of bedding dip after tilt correction of Euro Basalt.

Unit	ID	<i>N</i>	<i>Dg</i> (°)	<i>Ig</i> (°)	<i>k</i>	α_{95} (°)	<i>R</i>	<i>Ds</i> (°)	<i>Is</i> (°)	<i>Dss</i> (°)	<i>Iss</i> (°)
All specimens	DOP	125	129.0	−52.3	17.61	2.9	118.0	–	–	–	–
Euro Basalt	EBp	8	349.4	−20.8	56.9	7.4	7.87	344.8	47.6	–	–
Euro Basalt	EBm	16	316.3	−40.7	51.6	5.2	15.71	327.2	16.5	–	–
Coucal/Double Bar	CDp	7	005.9	−11.1	15.5	15.8	6.61	010.2	58.5	125.4	6.9
Coucal/Double Bar	CDm	22	016.8	7.9	9.8	10.4	19.86	054.9	70.5	083.7	39.0

4. Paleomagnetism

We prepared all paleomagnetic specimens using water-cooled, nonmagnetic equipment and stored and measured them in a magnetically shielded room (<150 nT DC field) in the MIT Paleomagnetism Laboratory. Samples were stored for two months prior to demagnetization to allow for the decay of any viscous remanent magnetization (VRM). We cut each sample into mutually-oriented cylindrical specimens (~5 cm³ each) and wedge-shaped end chips (1–3 cm³ each). Remanence measurements were acquired with the SRM equipped with an automatic sample handler, alternating field (AF) demagnetizer, and rock magnetism analysis system (Kirschvink et al., 2008). We reconstructed the in situ sample orientations using Ballmark™ orientation lines scribed on core segments during extraction, correcting for down-core variation in drill core azimuth and inclination from 310 to 320° and 60 to 59°, respectively. NRM intensities of the specimens were typically $\sim 5 \times 10^{-3}$ A/m, but ranged between 1×10^{-5} and 1×10^{-1} A/m. The average observed intensity is several orders of magnitude weaker than modern fresh basalts, but is typical for altered Archean metabasalts (Biggin et al., 2011; Strik et al., 2003; Yoshihara, 2001).

We subjected all paleomagnetic specimens to progressive AF demagnetization up to 20 mT in 1 mT increments, followed by progressive thermal demagnetization in temperature increments of 5–20 °C up to 600 °C or until the limit of reproducible measurements. We measured the low field susceptibility of each sample after each thermal step using a Bartington MS-1 Magnetic Susceptibility System. In some specimens, particularly in the sub-unconformity alteration zone, erratic demagnetization above 350 °C coincided with a large increase in low-field susceptibility, presumably due to laboratory oxidation of iron sulfides. We calculated principal component analysis line, great circle, and small circle fits (Kirschvink, 1980; Mardia and Gadsden, 1977) to demagnetization vector endpoint data using the software of Cogné (2003) and Jones (2002). Mean directions and their associated 95% confidence intervals were calculated using Fisher statistics, after applying the quantile–quantile method to confirm that the data are Fisher-distributed (Tauxe, 2010); Table 1. We define origin-trending components as having least squares line fit directions whose angular deviation from the origin (DANG) values are less than their maximum angular deviation (MAD) values, indicating that no additional component is required to explain the paleomagnetic remanence (Tauxe and Staudigel, 2004). A subset of Double Bar and Coucal Formation specimens exhibited wild demagnetization paths at temperatures above 500 °C due to chemical alteration. For these specimens, we resort to forcing a linear fit from the origin through the cluster of highest temperature, stable vector endpoints (Fig. 4).

We identified up to three well-characterized magnetization components in igneous samples (Fig. 4A; Tables S1–S5), but found that the silicified sedimentary rocks of the Strelley Pool Formation lacked a stable magnetization. In all igneous samples, we identified an up-core drilling overprint (DOP) that was mostly removed

by progressive AF demagnetization up to peak fields of 20 mT (Fig. 4B), although in a few specimens this overprint persisted to high temperatures during subsequent thermal demagnetization. We also identified origin-trending components that unblocked between 280–570 °C in 102 specimens from both the Euro Basalt and Coucal Formation/Double Bar Formation, respectively denoted EBm and CDm (Fig. 4C, D). The well-defined maximum unblocking temperatures for EBm and CDm components are consistent with the rock magnetic indications of the dominance of fine-grained, low-Ti titanomagnetite as magnetic carriers. For 31 specimens, we additionally observed significant demagnetization between 280–350 °C, which we attribute to the presence of titanomaghemite, high-Ti titanomagnetite, or pyrrhotite (see Section 3). We refer to the linear components fit to the temperature range of 250–400 °C as EBp and CDp, respectively (Fig. 4F).

5. Core orientation

5.1. ABDP-8 core

Equal area stereonet projections of the EBm component fits reveal a cluster of directions pointing northwest-up that is intersected by a well-defined scatter of directions that fall within a narrow annulus about a small circle (Fig. 4C). The best-fit pole to this small circle closely approximates the up-core direction, indicating that many of the sampled core segments were misoriented due to spinning of core segments during cutting and subsequent improper extrapolation of the Ballmark™ orientation line during sub-sampling. A detailed discussion of this issue is presented in the [Supplementary information](#). Physical inspection of the quarter core at ASU after completion of the demagnetization program and examination of post-quartering photographic core logs verified that all samples taken from core segments that can be physically linked to segments bearing the original Ballmark™ orientation mark (Fig. 4C, red symbols) fall within the “non-spun” cluster, while all “spun” samples are separated by breaks in the drill core across which core orientation is lost. Therefore, we can confidently identify the cause of the excess scatter and exclude the spun EBm directions.

Much of the dispersion of the CDm component is also due to drill core misorientation. A small circle fit to the CDm directions has low error and yields a pole that closely coincides with the drilling axis (Fig. 4D). Bedding orientations of planar-laminated cherts calculated from the angles at which they intersect the core show a progressive clockwise shallowing of dip that is consistent with rotation of steeply southeast-dipping beds about the drilling axis, which would yield progressively shallower apparent dips with larger amounts of core misorientation, as is observed (Fig. 4D, blue symbols). Directions from the stratigraphically lowest cherts span the entire CDm scatter but are derived from only a few meters of fragmented core. We therefore also interpret the CDm scatter as the result of drill core spinning of a single component that lies in the northeast-equatorial/down direction. As with the Euro Basalt,

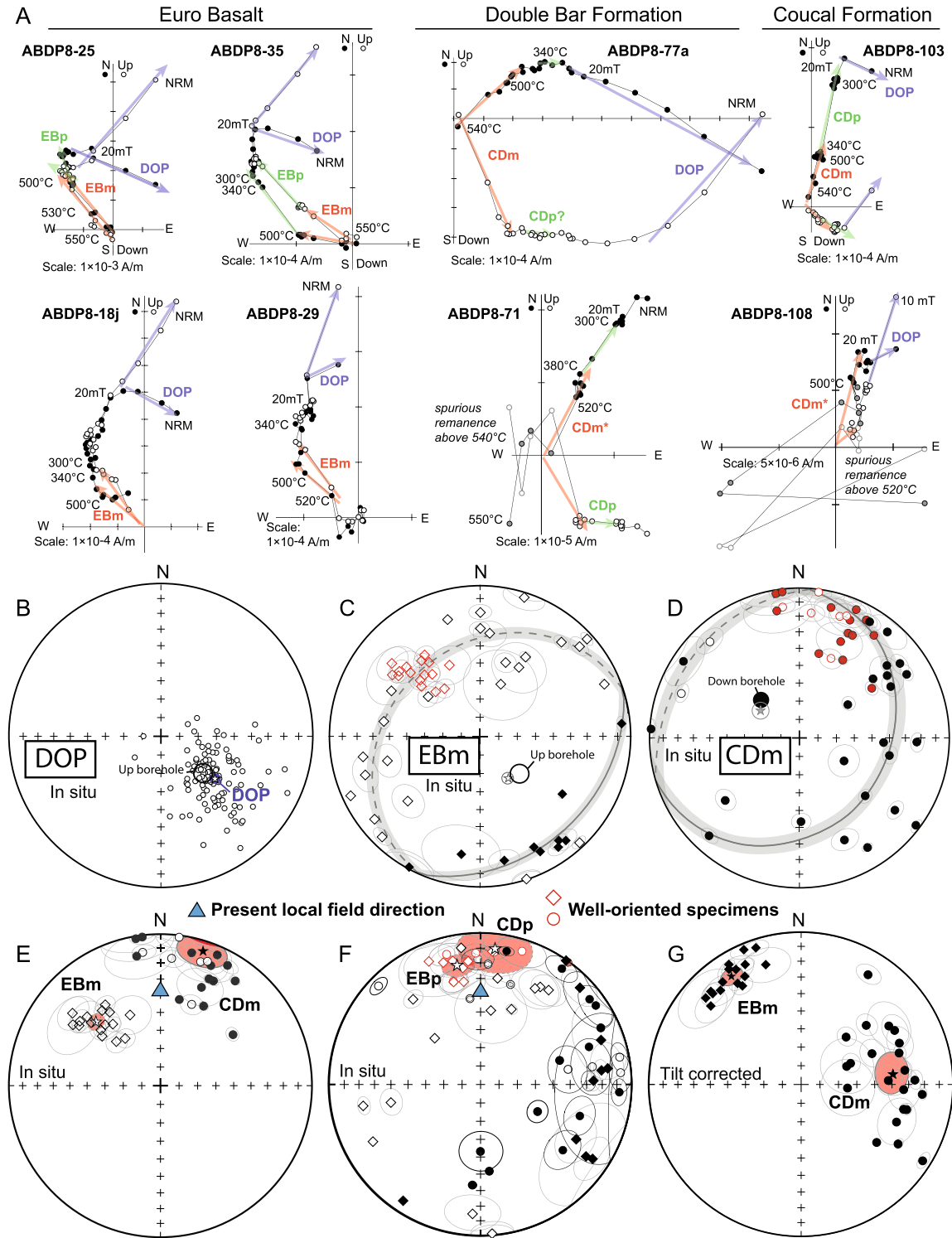


Fig. 4. Paleomagnetic measurements. (A) Vector endpoint diagrams in geographic coordinates for representative specimen demagnetizations. Colored arrows indicate linear component fits. The CDm* component is calculated by forcing a best-fit line through the origin and a cluster of vector endpoints for specimens that became magnetically unstable during heating above 500°C. (B) Great circles and combined best-fit points calculated from low-field (<20 mT) AF demagnetization paths for all ABDP-8 specimens. The estimated mean direction of the removed component (DOP) parallels the up-hole direction of the drill core (black circle). (C, D) Equal-area stereographic projections of EBm and CDm component fits. Green small circles, dashed in the upper hemisphere and solid in the lower hemisphere, indicate best-fit planes of the EBm (C) and CDm (D) directions and the annulus of 95% confidence (Mardia and Gadsden, 1977). Green stars indicate the position of the best-fit poles for these planes and are surrounded by ellipses of 95% confidence. Red symbols indicate specimens for which accurate Ballmark™ orientation has been verified by inspection of the core housed at ASU. Blue symbols in (D) indicate specimens of Coucal Formation banded chert and are labeled with the magnitude of bedding dip calculated from intersection angles of planar chert beds with the core. Shallow inferred dips are associated with spun specimens due to the oblique intersection of the drill core with bedding at depth. (E) High-temperature component EBm (diamonds) and CDm (circles) fits and their Fisher mean directions (stars) and associated 95% confidence intervals (red ellipses) after exclusion of misoriented specimens. Triangle shows present local field direction. (F) Low-temperature component EBp (diamonds) and CDp (circles) fits and their Fisher mean directions (stars) and associated 95% confidence intervals (red ellipses) after exclusion of misoriented specimens. (G) EBm (diamonds) and CDm fits (circles) and their Fisher mean directions (stars) and associated 95% confidence intervals (red ellipses) after correction for local tilting in two stages. (For interpretation of the references to color in this figure legend, the reader is referred to the web version of this article.)

physical identification of confidently Ballmark™-oriented core fragments guided rejection of spun samples (Fig. 4D, red symbols).

After exclusion of misoriented specimens, we identified clustered EBp and EBm directions and distinct, clustered CDp and CDM directions (Fig. 4E, F). Curved trajectories in vector end-point diagrams indicate that for 10 Euro Basalt samples, the DOP overlapped the EBm component at blocking temperatures below 450 °C. For these samples, we estimated the EBm components using great circle fits, but due to uncertainties in core orientation we do not include them in the EBm mean direction. We tested the component mean directions for similarity to each other using Watson's test for the common mean, in which the critical p -value is calculated from the F distribution with 2 and $2(N - 2)$ degrees of freedom for N total measurements (Watson, 1956). The EBm direction is distinct from the present local field direction (PLF), CDm, CDp, and EBp at >99.9% confidence. The CDp direction is distinct from CDm at 90% confidence and EBp at 80% confidence. The similarity of the CDp and EBp directions to the PLF direction suggests that they represent a viscous overprint by the modern geomagnetic field.

5.2. Comparison with ABDP-1 core

Achieving accurate core orientation has been a persistent technical obstacle to paleomagnetic studies utilizing subsurface drilling. Paleomagnetic measurements of the ABDP-1 drill core, which was also drilled into a Paleoproterozoic supracrustal sequence in the East Pilbara craton, yielded apparent evidence for fast plate motion relative to an assumed stationary geomagnetic dipole field during deposition of the ~3460 Ma Marble Bar Chert (Suganuma et al., 2006). This record of paleomagnetic remanence has been considered to be one of the most reliable thus reported from the Paleoproterozoic of the East Pilbara craton (Biggin et al., 2011). However, upon reexamination of the published data, we find that this variation is best explained by minor misorientation of drill core segments (Fig. S2), which were oriented after extraction by matching the bedding in core segments to the orientation of bedding at the surface, by assuming a uniform bedding tilt at depth. A small circle with a pole equivalent to the drill hole orientation (plunging 40° toward azimuth 230°) can be fit to the in-situ data (recovered by back-rotation of the published tilt-corrected binned averages about the strike/dip 323°/83°, overturned), leading us to suggest that low-amplitude folding in the subsurface chert resulted in misorientation of the drill core progressively with depth. We interpret the published binned-mean direction MB1, which was derived from the shallowest and most reliably oriented part of the core, as the best estimate of the paleomagnetic remanence of the Marble Bar Chert.

6. Tilt correction

We determined the overall bedding orientation of the sampled units by correlating the steeply-dipping chert beds present in overlying outcrops (Fig. 1A) with those observed at depth in the drill core (Fig. 1B). The resulting bedding orientations are consistent with surface exposures as well as with individual bedding orientations calculated from intersection angles of semi-planar chert bedding in well-oriented core segments. The Euro Basalt samples were tilt-corrected using the bedding dip direction/dip 181°/70° under the assumption that deformation was primarily driven by radial tilting away from the Carlinde granitoid complex rather than the development of the southwestward-plunging Pilgangoora Syncline megafold, which increases dramatically in intensity of folding and metamorphism ~30 km westward of the ABDP-8 drill site. This correction is supported by the observation that radial un-tilting of syn-depositional normal faults affecting the stratigraphic interval

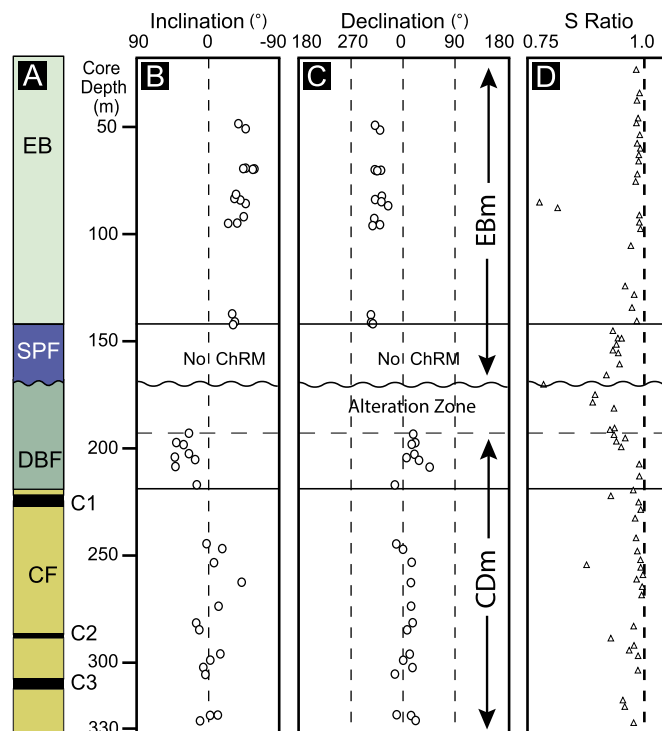


Fig. 5. Magnetic stratigraphy of ABDP-8 core. (A) Geologic stratigraphy of core. EB = Euro Basalt, SPF = Strelley Pool Formation, DBF = Double Bar Formation, CF = Coucal Formation. (B, C) Variation of in-situ remanent magnetization with depth for accurately oriented specimens. (D) Variation of the forward S ratio with depth.

containing the Euro Basalt recovers a consistent east–west regional extension direction throughout the East Pilbara Craton (de Vries et al., 2006), a result that holds at the ABDP-8 site. We applied the same initial tilt correction to the Double Bar and Coucal directions, followed by a further tilt-correction of the remaining bedding dip direction/dip 102°/36° to account for the bedding cutoff angle observed along the sub-Strelley Pool Formation unconformity at the drill site. Even after exclusion of misoriented specimens, the scatter of CDm directions exhibits a strong preferred direction that mimics the expected scatter due to drill core misorientation. However, we note that the direction of this elongation of scatter is also consistent with post-magnetization folding of the Coonterunah Group, which is observed in surface outcrops. Because the exact geometry of subsurface folds is unknown, we consider the second tilt correction to be approximate in nature and we do not consider the CDm direction to be well-constrained.

7. Magnetostratigraphy

A plot of in situ magnetic declination and inclination versus down-core depth reveals a sharp (87°) change in the direction of the in-situ high-temperature magnetization, from the CDm to the EBm component, that occurs across the stratigraphic interval containing the sub-Strelley Pool Formation unconformity (Fig. 5). The Double Bar Formation exhibits a dramatic decrease in the forward S-ratio within 25 m of the unconformity, coincident with a loss of resolvable CDm magnetic components during thermal demagnetization and an increased percentage of dispersed iron sulfide (pyrite) minerals. This relationship suggests that the sub-aerially exposed ground surface was subjected to weathering by an oxygen-poor atmosphere, leading to pyrite growth possibly at the expense of remanent titanomagnetite. Inclusion of white micas within large pyrite grains shows that sulfide growth postdated or coincided with this intense alteration event.

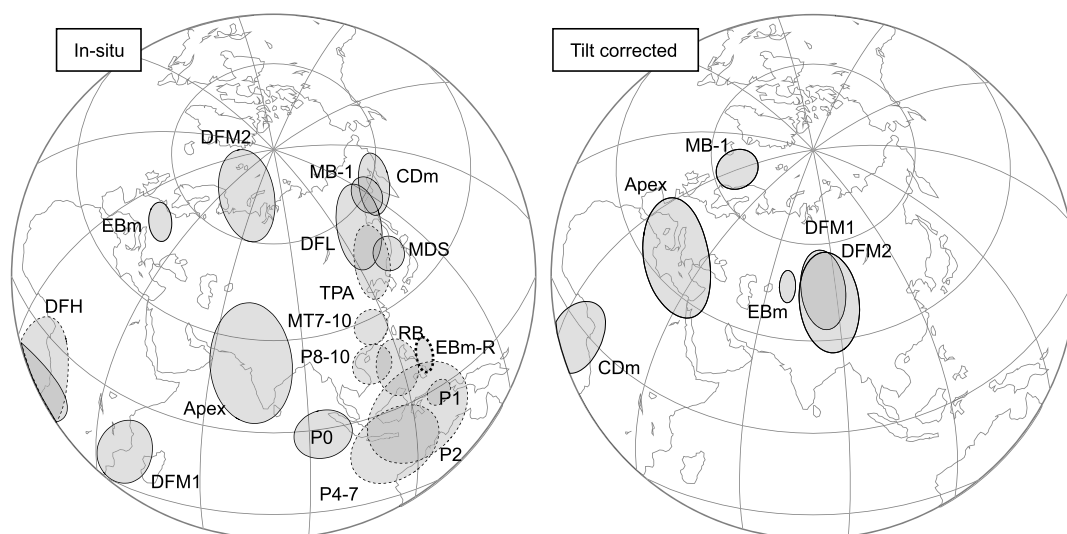


Fig. 6. Paleoproterozoic and Neoproterozoic paleomagnetic poles from the East Pilbara craton. Left panel shows in-situ remanences of Paleoproterozoic rock units compared with the position of the Neoproterozoic APW path. EBm-R indicates the position of the reversed-polarity EB-m paleopole. Right panel shows distribution of Paleoproterozoic poles after correction for local structural tilt. Dashed ellipses indicate lower-hemisphere projections. Labels and source references are presented in the online [supplement](#).

Undersampling of the secular variation of the geomagnetic field can result in high-precision paleomagnetic mean directions that only represent the instantaneous paleofield direction, while strong averaging of secular variation over long time intervals can result in high-precision paleomagnetic mean directions that do accurately reflect the time-averaged paleofield direction. As the EBm and CDm magnetizations appear to be chemical remanent magnetizations and are clearly not primary thermoremanent magnetizations, they probably integrate the field direction over time periods much longer than the $\sim 10,000$ year interval that is required to average paleosecular variation in Phanerozoic rocks. Thus, we do not expect that higher frequency records of the Paleoproterozoic geomagnetic field are reflected in our measurements.

8. Age of magnetizations

Preservation of primary thermoremanent magnetizations within volcanic rocks of Paleoproterozoic age is unlikely, because of the individual or combined effects of seafloor hydrothermal alteration, local and regional metamorphism, orogenic fluid flow, deep cratonic weathering, and the expected decay of remanence over very long timescales. Nevertheless, we observe consistencies of remanence directions within the ABDP-8 drill core over stratigraphic thicknesses of >100 m both above and below the unconformity, which strongly suggests preservation of two ancient paleofield directions. Because our knowledge of potential paleomagnetic overprints is incomplete and we do not have access to a fold test or conglomerate test for dating the observed remanence, we must adopt the approach of addressing the known overprinting events as potential explanations of our observations. We propose three alternative scenarios that have very different implications for the meaning of the paleomagnetic record.

In the first scenario, the Euro Basalt was remagnetized long after it was emplaced while the Coonterunah Subgroup avoided this late remagnetization event. The most likely timing for remagnetization of the Euro Basalt would be coincident with eruption of the Neoproterozoic Fortescue Group, similar to widespread remagnetizations observed in the Kaapvaal craton due to the emplacement of the Jurassic Karoo Large Igneous Province (Strik et al., 2007). Some difference in porosity or mineralogy, or aquitard behavior of the Strelley Pool Formation, would have allowed the magnetization of the Coonterunah Group rocks to remain unaffected by this overprint. This scenario is hinted at by the similarity the

in situ EBm-R (reversed polarity) virtual geomagnetic pole (VGP) with the <2700 Ma reach of the published Neoproterozoic apparent polar wander (APW) path for the East Pilbara craton (Fig. 6), as defined by the location of the ~ 2718 Ma P8-10 and undated (<2715 Ma, >1700 Ma) MT paleopoles (Strik et al., 2003). The location of the EBm-R pole along this portion of the Neoproterozoic APW path, and not the significantly different and better constrained ~ 2770 Ma portion, or near the P0 pole derived from the oldest Fortescue Group flood basalts in this region (Strik et al., 2003) suggests that the proposed, post-deformation bedrock remagnetization of the East Strelley Belt would have significantly postdated initial eruption of the earliest flood basalts and emplacement of large feeder dykes around ~ 2772 Ma. These Neoproterozoic units are not known to be overprinted by ~ 2718 Ma or MT directions, and the MT overprint that does affect P7-10 units is restricted to temperature ranges of 350 – 450 °C (Strik et al., 2003). Near Marble Bar, emplacement of the basal Fortescue Group did not remagnetize the immediately underlying rock substrate, which consists of altered basalts very similar in lithology and age to the units sampled by the ABDP-8 core (Suganuma et al., 2006; Yoshihara, 2001). Although it is possible that the MT overprint observed in the upper Fortescue Group units represents a regional overprint that was more intensely developed within the East Strelley Belt than in the Marble Bar region and is recorded by EBm, we are not aware of any geological rationale for such an event.

Overprinting of the Euro Basalt could also have potentially occurred during regional transpression that accompanied development of the Lalla Rookh – Western Shaw structural corridor at ~ 2940 Ma (Van Kranendonk and Collins, 1998). However, no simple structural correction of the Euro Basalt can align the in situ EBm-R paleopole with the earliest paleopoles that define the >2770 Ma Neoproterozoic APW path.

In the second scenario, the magnetization of the Euro Basalt significantly predates that of the Coonterunah Group. The Euro Basalt remanence could be as old as an early chemical remanent magnetization due to seafloor alteration, or as young as a Neoproterozoic overprint. To date, the only reported overprinting event with a pole location similar to that derived from the in-situ CDm magnetization direction is associated with emplacement of the Mundine Wells Dyke Swarm (MDS) (Fig. 6). This is a 755 ± 3 Ma set of doleritic dykes that extend from the western Yilgarn craton into the East Pilbara craton (Wingate and Giddings, 2000). Positive baked contact tests indicate that thermal

remagnetization associated with intrusion of MDS dykes into the uppermost crust does not extend more than several hundred meters from the dykes (Wingate and Giddings, 2000), which have not been mapped within tens of kilometers of the ABDP-8 drill site. Because any regional magnetic overprint sufficient to reset the Coonterunah Subgroup rocks with a consistent remanence should also be apparent as an overprint of the Euro Basalt, we do not believe that the rock magnetic or paleomagnetic data warrants this scenario.

In the third scenario, the EBm and CDm magnetizations are both Paleoproterozoic in age, and the abrupt change in magnetization direction is a primary feature of the rock column dating to the time gap represented by the unconformity underlying the Strelley Pool Formation as well as the period of deposition of the Strelley Pool Formation itself. The Coonterunah Group volcanics could either preserve a magnetization acquired soon after emplacement, or more likely, a magnetic overprint acquired during greenschist-facies metamorphism prior to exposure of the units to subaerial erosion. The Euro Basalt magnetization would most likely represent a chemical remanent magnetization acquired during early seafloor hydrothermal alteration, when the low-grade bulk mineralogy of the Euro Basalt was developed. Upon tilt correction (Fig. 6), the EBm paleopole nearly coincides with the pole reported from the ~3460 Ma Duffer Formation (DUF) of the East Pilbara craton (McElhinny and Senanayake, 1980); these poles also fall relatively close to the supposed Paleoproterozoic paleopoles reported from the Marble Bar Chert and Apex Basalt (Suganuma et al., 2006; Yoshihara, 2001).

While the complete and exclusive alteration and remagnetization of the metavolcanic units either beneath or above the angular unconformity well after emplacement of the Euro Basalt cannot be comprehensively ruled out by our observations, we propose that the third scenario is the most likely. In this model, the magnetization of each metavolcanic rock was acquired during the latest major alteration or metamorphism experienced by that rock, and the step change in magnetization direction seen in the ABDP-8 core corresponds with the time gap represented by the intervening erosion surface and sedimentary cover. For the purposes of the following discussion, we assume that the CDm magnetization was acquired between ~3515 Ma and ~3350 Ma, placing it within the range of the oldest known terrestrial magnetizations, and the EBm magnetization was acquired soon after ~3350 Ma.

9. Discussion

9.1. Paleoproterozoic geomagnetism and climate

The Strelley Pool Formation preserves some of the oldest putative biogenic stromatolites and microbial microfossils (Allwood et al., 2006; Lowe, 1980; Wacey, 2010; Wacey et al., 2011). Partially silicified laminites covering ~30,000 km² areal extent (Hickman, 2008) record the widespread development of a shallow-water carbonate platform (Lowe, 1983) that is unique in the Paleoproterozoic sedimentary record and is one of the earliest examples of an evaporitic paleo-environment. The common occurrence of primary and diagenetic evaporites indicates supersaturation due to periodic basin restriction (Hofmann et al., 1999; Lowe, 1983), and sedimentary structures characteristic of tidal action (de Vries et al., 2010) support a periodic connection to the open ocean. In the modern climatic context, this close association of evaporites and platform carbonates in a marginal marine setting would be most consistent with deposition at lower than ~30° latitude (Briden, 1970; Kiessling et al., 2003). Isotopic analyses of sedimentary rocks preserved in the Barberton Belt of South Africa suggest that the temperature of the shallow ocean near Earth's equator at the time of deposition of the

Strelley Pool Formation was less than 35–40 °C (Hren et al., 2009; Blake et al., 2010), comparable to temperatures of over 28–32 °C estimated for Cretaceous to Eocene time (Pearson et al., 2001) and not sufficiently hot to demand a non-uniformitarian climate zonation.

Because there is a conformable (Van Kranendonk, 2006) and locally interfingering (de Vries et al., 2010) contact between the Euro Basalt and the underlying Strelley Pool Formation, a steep EBm component would be inconsistent with magnetization under modern (post-2000 Ma) climatic conditions. Following structural correction, the EBm component has a shallow inclination that would correspond with magnetization at low paleolatitude ($7.7 \pm 2.5^\circ$) under the assumption of a GAD field. This is consistent with the combined hypotheses of uniformitarian climate zonation, orbital obliquity, and GAD field geometry during deposition of Earth's oldest known carbonate platform. However, it does not require any of these three hypotheses to be true individually.

9.2. Paleoproterozoic Vaalbara

The consistency of paleopole directions reported from low-grade sequences in the Barberton Greenstone Belt strongly suggests at least local preservation of Paleoproterozoic geomagnetic field directions (Biggin et al., 2011). Directionally similar magnetizations of Paleoproterozoic age also appear to persist within low-grade sequences of the East Pilbara craton with emplacement ages spanning ~150 Myr. The presently available data are insufficient to resolve whether these gross directional similarities result from yet-unresolved regional remagnetizations in both cratons or from low latitudinal drift rates that might reflect early plate tectonic processes. As discussed by Biggin et al. (2011), Paleoproterozoic paleopoles from the East Pilbara craton overlap with nearly coeval poles from the Kaapvaal craton after application of the Zegers et al. (1998) or de Kock et al. (2009) reconstructions of Neoproterozoic Vaalbara (compare Fig. 7A and B). The tilt-corrected Euro Basalt paleopole determined in our study falls within this broad cluster of poles under either reconstruction, and is thus broadly consistent with the Paleoproterozoic Vaalbara hypothesis.

Markedly similar ~3500–3300 Ma stratigraphic sequences exposed on both cratons (Fig. 7C, D) record a transition from deep-water volcanism to shallow-water sedimentation and local development of high-relief erosional unconformities (Buick et al., 1995; de Vries et al., 2010; de Wit et al., 2011). With the addition of the Euro Basalt paleopole from this study, these sequences are also bracketed by paleomagnetic poles indicating deposition in close proximity under the Neoproterozoic Vaalbara reconstruction (de Kock et al., 2009). Comparison of lithological descriptions and igneous and detrital U/Pb zircon ages from both sequences (Barley et al., 1998; Byerly et al., 1996; de Vries, 2004; de Vries et al., 2006; de Wit et al., 1987; Grosch et al., 2011; Kröner et al., 1991; Kröner and Todt 1988; Nelson, 1998, 2001, 2002, 2004, 2005; Thorpe et al., 1992) indicates that they developed coevally and that direct correlation of the similar lithological units as well as the regional unconformities cannot yet be ruled out (Fig. 7C, D and Table S6). The seemingly independent records of mantle evolution, tectonic style, and the development of early microbial life inferred from the geological record of the East Pilbara and Kaapvaal cratons may therefore be aspects of the evolution of a single crustal mass (Biggin et al., 2011).

9.3. Summary

Paleomagnetic studies of drill core offer unprecedented access to records of ancient remanent magnetization that are largely unavailable from weathered and lightning-remagnetized surface sam-

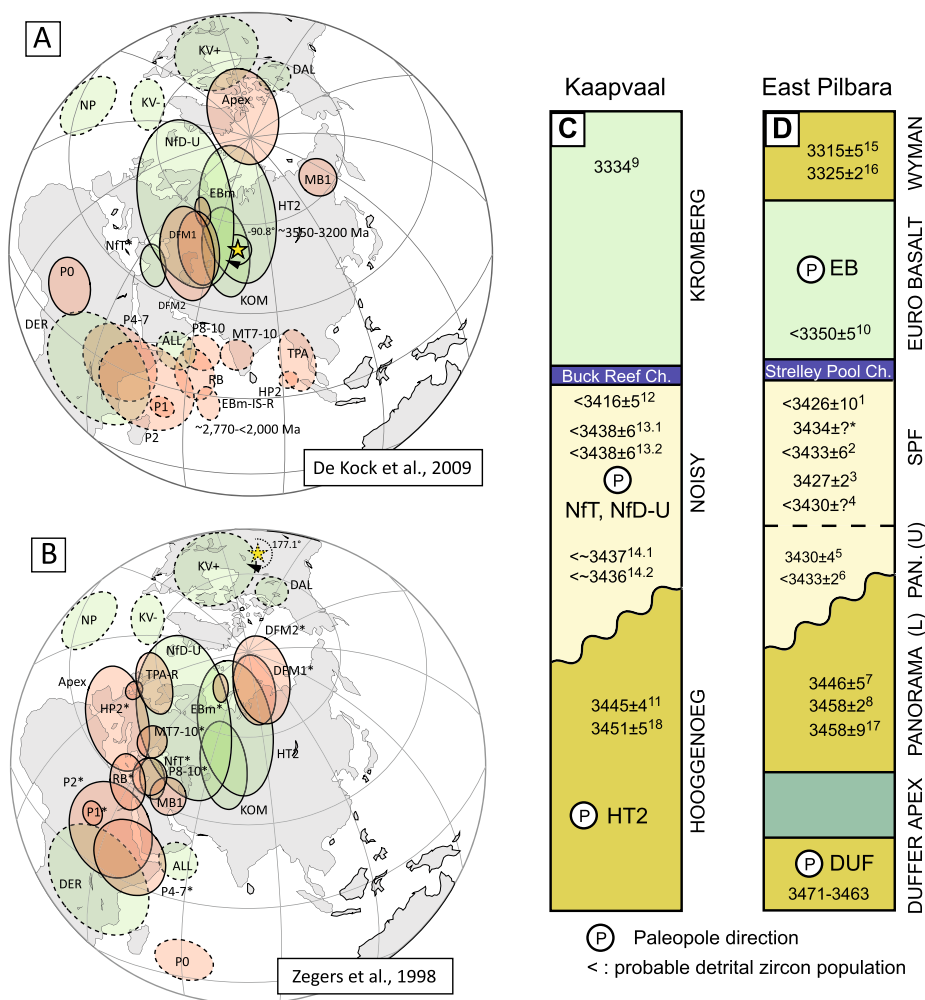


Fig. 7. Paleomagnetic and stratigraphic data suggestive of a Paleoproterozoic Vaalbara (McElhinny and Senanayake, 1980; Hale and Dunlop, 1984; Schmidt and Embleton, 1985; Schmidt and Clark, 1994; Laver et al., 1998; Wingate, 1998; Li, 2000; Wingate and Giddings, 2000; Yoshihara, 2001; Strik et al., 2003; Suganuma et al., 2006; Tarduno et al., 2007; de Kock et al., 2009; Biggin et al., 2011). Asterisks indicate poles that have been reversed in polarity. VGP data are given in the online supplement. Stars: Pole of rotation for applied reconstruction of Neoproterozoic Vaalbara. (A) Paleoproterozoic and Neoproterozoic pole alignment after reconstruction of the de Kock et al. (2009) Neoproterozoic Vaalbara. (B) Paleoproterozoic pole alignment after reconstruction of the Zegers et al. (1998) Neoproterozoic Vaalbara. (C, D) Composite stratigraphic columns (not to scale) of supracrustal successions bracketing the oldest known erosion surfaces from the (C) Kaapvaal craton (Hooggenoeg, Noisy, and Kromberg Formations) and (D) East Pilbara craton (Duffer, Apex, Panorama, Strelley Pool, Euro, and Wyman Formations). Shown are radiometric age constraints, with superscripts indicating data sources given in Table S6, and the stratigraphic positions of inferred Paleoproterozoic magnetic remanences. Age constraints for sediments blanketing the unconformities are from zircons thought to be detrital.

ples. The ABDP-8 core in particular provides a consistency test (although not proof) for modern-style climatic zoning, low orbital obliquity, and GAD field geometry in the Paleoproterozoic. The paleomagnetic directions also support the hypothesis that two of the great Paleoproterozoic terranes that have survived to the present day were linked during their earliest periods of formation. We expect that the continued exploration of other deep drill cores will continue to yield important new constraints on the tectonics, paleogeography, climate and geomagnetism on the early Earth.

Acknowledgements

The core drilling was funded by a NASA Astrobiology Institute grant to RB and its analysis was supported by a NSF Geophysics Program grant to BPW (#0408928). We thank P and JP van Loenhout of Mt Magnet Drilling for core acquisition and LC Bonser and JSR Dunlop for Ballmarking. This manuscript benefited from insightful and challenging reviews from D.A.D. Evans, Andrew Biggin, and an anonymous reviewer.

Appendix A. Supplementary material

Supplementary material related to this article can be found online at <http://dx.doi.org/10.1016/j.epsl.2015.03.008>.

References

- Allwood, A.C., Walter, M.R., Kamber, B.S., Marshall, C.P., Burch, I.W., 2006. Stromatolite reef from the Early Archaean era of Australia. *Nature* 441 (7094), 714–718.
- Barley, M., Loader, S., McNaughton, N., 1998. 3430 to 3417 Ma calc-alkaline volcanism in the McPhee Dome and Kelly Belt, and growth of the eastern Pilbara craton. *Precambrian Res.* 88 (1), 3–23.
- Biggin, A.J., de Wit, M.J., Langerer, C.G., Zegers, T.E., Voute, S., Dekkers, M.J., Drost, K., 2011. Palaeomagnetism of Archaean rocks of the Onverwacht Group, Barberton Greenstone Belt (southern Africa): evidence for a stable and potentially reversing geomagnetic field at ca. 3.5 Ga. *Earth Planet. Sci. Lett.* 302 (3–4), 314–328. <http://dx.doi.org/10.1016/j.epsl.2010.12.024>.
- Blake, R.E., Chang, S.J., Lepland, A., 2010. Phosphate oxygen isotopic evidence for a temperate and biologically active Archaean ocean. *Nature* 464 (7291), 1029–1032.
- Blewett, R.S., 2002. Archaean tectonic processes: a case for horizontal shortening in the North Pilbara Granite-Greenstone Terrane, Western Australia. *Precambrian Res.* 113, 87–120.
- Briden, J., 1970. Palaeolatitude distribution of precipitated sediments. In: Runcorn, S.K. (Ed.), *Palaeogeophysics*. Academic Press, New York, pp. 437–444.

- Buick, R., Thorne, J.R., McNaughton, N.J., Smith, J.B., Barley, M.E., Savage, M., 1995. Record of emergent continental crust ~3.5 billion years ago in the Pilbara craton of Australia. *Nature* 375, 574–577.
- Byerly, G.R., Kröner, A., Lowe, D.R., Todt, W., Walsh, M.M., 1996. Prolonged magmatism and time constraints for sediment deposition in the early Archean Barberton greenstone belt: evidence from the Upper Onverwacht and Fig Tree Groups. *Precambrian Res.* 78 (1), 125–138.
- Carpenter, L., Weiss, B.P., Gilder, S.A., Pommier, A., Hart, R.J., 2012. Lightning remagnetization of the Vredefort impact crater: no evidence for impact generated magnetic fields. *J. Geophys. Res., Planets* 117, E01007.
- Cheney, E., Roering, C., Stettler, E., 1988. In: *Vaalbara: Geocongress '88*. Durban, pp. 85–88.
- Cisowski, S., 1981. Interacting vs. non-interacting single domain behavior in natural and synthetic samples. *Phys. Earth Planet. Inter.* 26 (1–2), 56–62.
- Cogné, J., 2003. PaleoMac: a Macintosh™ application for treating paleomagnetic data and making plate reconstructions. *Geochim. Geophys. Geosyst.* 4 (1), 1007.
- de Kock, M.O., Evans, D.A.D., Beukes, N.J., 2009. Validating the existence of Vaalbara in the Neoproterozoic. *Precambrian Res.* 174 (1–2), 145–154. <http://dx.doi.org/10.1016/j.precamres.2009.07.002>.
- de Vries, S.T., 2004. Early Archean sedimentary basins: depositional environment and hydrothermal systems; examples from the Barberton and Coppins Gap Greenstone Belts. *Geol. Ultralectina* 244.
- de Vries, S.T., Nijman, W., Wijbrans, J.R., Nelson, D.R., 2006. Stratigraphic continuity and early deformation of the central part of the Coppins Gap Greenstone Belt, Pilbara, Western Australia. *Precambrian Res.* 147 (1–2), 1–27.
- de Vries, S.T., Nijman, W., de Boer, P.L., 2010. Sedimentary geology of the Palaeoarchaean Buck Ridge (South Africa) and Kittys Gap (Western Australia) volcano-sedimentary complexes. *Precambrian Res.* 183, 749–769.
- de Wit, M.J., Furnes, H., Robins, B., 2011. Geology and tectonostratigraphy of the Onverwacht Suite, Barberton greenstone belt, South Africa. *Precambrian Res.* 186 (1), 1–27.
- de Wit, M.J., Hart, R.A., Hart, R.J., 1987. The Jamestown ophiolite complex, Barberton mountain belt: a section through 3.5 Ga oceanic crust. *J. Afr. Earth Sci.* 6 (5), 681–730.
- Dunlop, D., Hanes, J., Buchan, K., 1973. Indices of multidomain magnetic behavior in basic igneous rocks: alternating-field demagnetization, hysteresis, and oxide petrology. *J. Geophys. Res.* 78 (8), 1387–1393.
- Dunlop, D.J., 2002. Theory and application of the Day plot (Mrs/Ms versus Hcr/Hc) 1. Theoretical curves and tests using titanomagnetite data. *J. Geophys. Res.* 107 (B3), 2056.
- Dunlop, D.J., Özdemir, Ö., 2001. *Rock Magnetism: Fundamentals and Frontiers*. Cambridge Univ. Press.
- Evans, D.A., 2006. Proterozoic low orbital obliquity and axial-dipolar geomagnetic field from evaporite palaeolatitudes. *Nature* 444, 51–55.
- Green, M.G., Sylvester, P.J., Buick, R., 2000. Growth and recycling of early Archean continental crust: geochemical evidence from the Coonterunah and Warrawoona Groups, Pilbara Craton, Australia. *Tectonophysics* 322 (1–2), 69–88.
- Grosch, E., Kosler, J., McLoughlin, N., Drost, K., Slama, J., Pedersen, R., 2011. Paleoproterozoic detrital zircon ages from the earliest tectonic basin in the Barberton Greenstone Belt, Kaapvaal craton, South Africa. *Precambrian Res.* 191 (1), 85–99.
- Hale, C.J., Dunlop, D.J., 1984. Evidence for an early Archean geomagnetic field: a paleomagnetic study of the Komati Formation, Barberton Greenstone Belt, South Africa. *Geophys. Res. Lett.* 11 (2), 97–100.
- Harnmeijer, J., 2009. Squeezing blood from a stone: inferences into the life and depositional environments of the early Archean. PhD thesis. University of Washington.
- Hickman, A.H., 2008. Regional review of the 3426–3350 Ma Strelley Pool Formation, Pilbara Craton, Western Australia. *Rec. - Geol. Surv. West. Aust.* 2008/15, 27 p.
- Hofmann, H.J., Grey, K., Hickman, A.H., Thorpe, R.I., 1999. Origin of 3.45 Ga coniform stromatolites in Warrawoona Group, Western Australia. *Geol. Soc. Am. Bull.* 111 (8), 1256–1262.
- Hren, M., Tice, M.M., Chamberlain, C.P., 2009. Oxygen and hydrogen isotope evidence for a temperate climate 3.42 billion years ago. *Nature* 462, 205–208. <http://dx.doi.org/10.1038/nature08518>.
- Johnson, H., Lowrie, W., Kent, D., 1975. Stability of ferromagnetic remanent magnetization in fine and coarse magnetite and maghemite particles. *Geophys. J. R. Astron. Soc.* 41 (1), 1–10.
- Jones, C.H., 2002. User-driven integrated software lives. *Comput. Geosci.* 28 (10), 1145–1151.
- Kiessling, W., Flügel, E., Golonka, J.A.N., 2003. Patterns of Phanerozoic carbonate platform sedimentation. *Lethaia* 36 (3), 195–225.
- Kirschvink, J., 1980. The least squares line and plane and the analysis of paleomagnetic data. *Geophys. J. R. Astron. Soc.* 62 (3), 699–718.
- Kirschvink, J.L., Kopp, R.E., Raub, T.D., Baumgartner, C.T., Holt, J.W., 2008. Rapid, precise, and high-sensitivity acquisition of paleomagnetic and rock-magnetic data: development of a low-noise automatic sample changing system for superconducting rock magnetometers. *Geochim. Geophys. Geosyst.* 9 (5), Q05Y01.
- Kitajima, K., Maruyama, S., Utsunomiya, S., Liou, J.G., 2001. Seafloor hydrothermal alteration at an Archean mid-ocean ridge. *J. Metamorph. Geol.* 19 (5), 583–599.
- Kröner, A., Byerly, G., Lowe, D., 1991. Chronology of early Archean granite-greenstone evolution in the Barberton Mountain Land, South Africa, based on precise dating by single zircon evaporation. *Earth Planet. Sci. Lett.* 103 (1–4), 41–54.
- Kröner, A., Todt, W., 1988. Single zircon dating constraining the maximum age of the Barberton greenstone belt, southern Africa. *J. Geophys. Res.* 93 (B12), 15329–15337.
- Kruiver, P.P., Passier, H.F., 2001. Coercivity analysis of magnetic phases in sapropel S1 related to variations in redox conditions, including an investigation of the S-ratio. *Geochim. Geophys. Geosyst.* 2, 2001GC000181.
- Layer, P.W., Lopez-Martinez, M., Kroner, A., York, D., McWilliams, M., 1998. Thermochronometry and palaeomagnetism of the Archean Nelshoogte Pluton, South Africa. *Geophys. J. Int.* 179, 850–872.
- Li, Z.X., 2000. Palaeomagnetic evidence for unification of the North and West Australian cratons by ca. 1.7 Ga: new results from the Kimberley Basin of north-western Australia. *Geophys. J. Int.* 142 (1), 173–180.
- Lowe, D.R., 1980. Stromatolites 3400-Myr old from the Archean of Western Australia. *Nature* 284 (5755), 441–443.
- Lowe, D.R., 1983. Restricted shallow-water sedimentation of Early Archean stromatolitic and evaporitic strata of the Strelley Pool Chert, Pilbara Block, Western Australia. *Precambrian Res.* 19 (3), 239–283.
- Lowrie, W., 1990. Identification of ferromagnetic minerals in a rock by coercivity and unblocking temperature properties. *Geophys. Res. Lett.* 17 (2), 159–162.
- Lowrie, W., Fuller, M., 1971. On the alternating field demagnetization characteristics of multidomain thermoremanent magnetization in magnetite. *J. Geophys. Res.* 76 (26), 6339–6349.
- Mardia, K., Gadsden, R., 1977. A small circle of best fit for spherical data and areas of vulcanism. *J. R. Stat. Soc., Ser. C, Appl. Stat.* 26 (3), 238–245.
- McElhinny, M.W., Senanayake, W.E., 1980. Paleomagnetic evidence for the existence of the geomagnetic field 3.5 Ga ago. *J. Geophys. Res.* 85 (Nb7), 3523–3528.
- Nelson, D.R., 1998. Compilation of SHRIMP U–Pb Zircon Geochronology Data, 1997. Geological Survey of Western Australia.
- Nelson, D.R., 2001. Compilation of Geochronology Data, 2000. *Geol. Surv. West. Aust.* 0730756947.
- Nelson, D.R., 2002. Compilation of geochronology data, 2001. *Geol. Surv. West. Aust.*
- Nelson, D.R., 2004. Compilation of geochronology data, 2004 update. *Geol. Surv. West. Aust.*, 0730756947.
- Nelson, D.R., 2005. Compilation of geochronology data, June 2005 update. *Geol. Surv. West. Aust.*
- Pearson, P.N., Ditchfield, P.W., Singano, J., Harcourt-Brown, K.G., Nicholas, C.J., Olsson, R.K., Shackleton, N.J., Hall, M.A., 2001. Warm tropical sea surface temperatures in the Late Cretaceous and Eocene epochs. *Nature* 413 (6855), 481–487.
- Saib, M.L., 1996. *Fundamentals of Atmospheric Physics*, vol. 61. Academic Press.
- Schmidt, P.W., Clark, D.A., 1994. Paleomagnetism and magnetic anisotropy of Proterozoic banded iron formations and iron ores of the Hamersley Basin, Western Australia. *Precambrian Res.* 69, 133–155.
- Schmidt, P.W., Embleton, B.J., 1985. Prefolding and overprint magnetic signatures in Precambrian (~2.9–2.7 Ga) igneous rocks from the Pilbara Craton and Hamersley Basin, NW Australia. *J. Geophys. Res., Solid Earth* 90 (B4), 2967–2984.
- Smithies, R.H., Champion, D.C., van Kranendonk, M.J., Hickman, A., 2007. Geochemistry of volcanic rocks of the northern Pilbara Craton. *Rep. - Geol. Surv. West. Aust.*, vol. 104, 47 p.
- Spiegel, D., Menou, K., Scharf, C., 2009. Habitable climates: the influence of obliquity. *Astrophys. J.* 691, 596–610.
- Strik, G., Blake, S., Zegers, T., White, S., Langereis, C., 2003. Palaeomagnetism of flood basalts in the Pilbara Craton, Western Australia: late Archean continental drift and the oldest known reversal of the geomagnetic field. *J. Geophys. Res.* 108 (B12), EPM 2-1–EPM 2-21.
- Strik, G., De Wit, M., Langereis, C., 2007. Palaeomagnetism of the Neoproterozoic Pongola and Ventersdorp Supergroups and an appraisal of the 3.0–1.9 Ga apparent polar wander path of the Kaapvaal Craton, Southern Africa. *Precambrian Res.* 153 (1–2), 96–115.
- Suganuma, Y., Hamano, Y., Niitsuma, S., Hoashi, M., Hisamitsu, T., Niitsuma, N., Kodama, K., Nedachi, M., 2006. Paleomagnetism of the Marble Bar Chert Member, Western Australia: implications for apparent polar wander path for Pilbara craton during Archean time. *Earth Planet. Sci. Lett.* 252 (3–4), 360–371.
- Tarduno, J.A., Cottrell, R.D., Watkeys, M.K., Bauch, D., 2007. Geomagnetic field strength 3.2 billion years ago recorded by single silicate crystals. *Nature* 446 (7136), 657–660.
- Tarduno, J.A., Cottrell, R.D., Watkeys, M.K., Hofmann, A., Doubrovine, P.V., Mamajek, E.E., Liu, Dunji, Sibeck, D.G., Neukirch, L., Usui, Y., 2010. Geodynamo, solar wind, and magnetopause 3.4 to 3.5 billion years ago. *Science* 327 (5970), 1238–1240.
- Tauxe, L., 2010. *Essentials of Paleomagnetism*. University of California Press, Berkeley, 489 p.
- Tauxe, L., Staudigel, H., 2004. Strength of the geomagnetic field in the Cretaceous Normal Superchron: new data from submarine basaltic glass of the Troodos Ophiolite. *Geochim. Geophys. Geosyst.* 5, Q02H06.
- Thorpe, R., Hickman, A.H., Davis, D., Mortensen, J., Trendall, A., 1992. U–Pb zircon geochronology of Archean felsic units in the Marble Bar region, Pilbara Craton, Western Australia. *Precambrian Res.* 56 (3–4), 169–189.

- Usui, Y., Tarduno, J.A., Watkeys, M., Hofmann, A., Cottrell, R.D., 2009. Evidence for a 3.45-billion-year-old magnetic remanence: hints of an ancient geodynamo from conglomerates of South Africa. *Geochem. Geophys. Geosyst.* 10 (9).
- Van Kranendonk, M., 2000. Geology of the North Shaw 1: 100,000 Sheet, Western Australia, 1: 100,000. Geological Series Explanatory Notes. Geol. Surv. West. Aust., Perth.
- Van Kranendonk, M.J., 2006. Volcanic degassing, hydrothermal circulation and the flourishing of early life on Earth: a review of the evidence from c. 3490–3240 Ma rocks of the Pilbara Supergroup, Pilbara craton, Western Australia. *Earth-Sci. Rev.* 74 (3–4), 197–240.
- Van Kranendonk, M.J., Collins, W.J., 1998. Timing and tectonic significance of late Archaean, sinistral strike-slip deformation in the central Pilbara structural corridor, Pilbara craton, Western Australia. *Precambrian Res.* 88 (1), 207–232.
- Wacey, D., 2010. Stromatolites in the ~3400 Ma Strelley Pool Formation, Western Australia: examining biogenicity from the macro- to the nano-scale. *Astrobiology* 10 (4), 381–395.
- Wacey, D., Kilburn, M.R., Saunders, M., Cliff, J., Brasier, M.D., 2011. Microfossils of sulphur-metabolizing cells in 3.4-billion-year-old rocks of Western Australia. *Nat. Geosci.* 4 (10), 698–702.
- Watson, G., 1956. Analysis of dispersion on a sphere. *Geophys. J. Int.* 7, 153–159.
- Wingate, M.T.D., 1998. A palaeomagnetic test of the Kaapvaal–Pilbara (Vaalbara) connection at 2.78 Ga. *S. Afr. J. Geol.* 101 (4), 257–274.
- Wingate, M.T.D., Giddings, J.W., 2000. Age and palaeomagnetism of the Mundine Well dyke swarm, Western Australia: implications for an Australia–Laurentia connection at 755 Ma. *Precambrian Res.* 100, 335–357.
- Xu, S., Dunlop, D.J., 1995. Toward a better understanding of the Lowrie–Fuller test. *J. Geophys. Res.* 100, 22.
- Yoshihara, A., 2001. Intensity of the Earth's magnetic field during the Archean. PhD thesis. University of Tokyo.
- Zegers, T., de Wit, M., Dann, J., White, S., 1998. Vaalbara, Earth's oldest assembled continent? A combined structural, geochronological, and palaeomagnetic test. *Terra Nova* 10, 250–259.

Supplementary Information for:
K. Bradley et al. (2015)
Records of geomagnetism, climate, and tectonics across a Paleoproterozoic erosion surface

Core misorientation

We examined photographic logs of the quartered drill core taken immediately after core sectioning was completed. This allows us to better constrain which specimens are from the lower part of each retrieved core section, and assess whether pieces of the intervening core can be clearly fit together or have fractured or missing sections.

The Ballmark orientation process uses a core break procedure to record the gravitationally lowest line on a core segment that lies within the drill string but has not yet been broken from the Earth. This procedure occurs once at the end of each ~6 m long core retrieval (commonly termed a “stick”). The Ballmark orientation is recorded on a plastic disc that is replaced before each drilling increment and this mark applies only to the broken segment (bottommost segment of each stick) and must be extrapolated to higher segments by matching of fractures within the core tray. Reliable Ballmark orientation requires a good break, adequate strength of the rock being broken allowing tensile stress to be transferred to a spring within the drill string, and proper propagation of the Ballmark orientation line from the lowest core segment through the other core segments of the same retrieval. This propagation can fail if the core segments are separated by fractures that cut orthogonally and not obliquely across the core, or if segment ends have rubbed against each other and worn away the surface of the fresh break. Finally, Ballmark indentations can be misinterpreted if an inner tensioning spring is compressed during string insertion or drilling, resulting in a false indentation on the plastic washer.

Within the ABDP-8 core, zones of crushed rock and gaps in core continuity are present in many core retrievals (Figure S3); however, a fiducial line was transcribed onto all core segments. We therefore must expect some of our specimens, which were collected without concern for potentially incorrect Ballmark lines, to be misoriented. An incorrect Ballmark measurement will result in systematic misorientation of one core retrieval. Incorrect matching of core fragments during extrapolation of the Ballmark line will result in systematic misalignment of the core segments above the improper match point. Core segments located nearest to the directly Ballmarked segment will tend to have better orientation than segments higher in the core stick. Core retrievals with few fractures, long core segments, and no missing sections will tend to be better oriented than highly fractured or non-recovered sections. Core retrievals with many small segments, rubble zones, or flat fractures will exhibit more misorientation.

We observe consistent magnetization directions within most core retrievals, with clear exceptions when core is missing or consists of rubble, indicating lack of a properly extrapolated fiducial line in the upper core segments (Figure S3). We identified 22 core retrievals that are most likely to have a proper Ballmark orientation. We include in the final EBm and CDM mean directions only the specimens that are most likely to represent well-oriented core.

Specimens collected from the core depth interval 302-313 meters have both bedding orientation and CDM components. Comparison of bedding poles with CDM directions shows that there is a clear correlation between the strike of bedding and the azimuth of the magnetization (Fig. S4). The pole to the best-fit small circle for the bedding poles closely approximates the down-core direction, as does the pole to the best-fit small circle for CDM components (Fig. S4). Hypothetical restoration of the bedding orientation for these to match the strike and dip of

bedding measured at the surface and extrapolated from the core intersection depth would result in northerly and shallowly plunging CDm directions that are similar to some of the CDm directions from the well-oriented core retrievals, but are clearly dissimilar from the EBm mean direction. However, because the bedding orientation at depth is unknown, we cannot unambiguously estimate the in-situ remanence of these specimens.

Table S1. EBm component fits

ID	<i>d</i> (m)	Spun?	<i>n</i>	Temp.	<i>Dg</i> (°)	<i>Ig</i> (°)	MAD (°)	<i>Ds</i> (°)	<i>Is</i> (°)
AB8-1	20.49	Y	8	400-528	021.6	-59.6	19.5	011.4	8.6
AB8-2	23.29	Y	13	440-565	307.2	-54.2	5.6	332.8	2.7
AB8-3	25.45	Y	5	440-520	137.0	-4.1	3.2	105.4	-44.3
AB8-4	26.53	Y	9	528-575	125.3	33.7	2.0	135.8	-14.5
AB8-5	29.46	Y	7	420-528	047.7	-4.5	3.1	068.0	38.0
AB8-6	31.57	Y	9	440-550	029.5	-39.0	2.8	025.2	25.2
AB8-7	34.34	Y	9	440-550	066.9	-11.4	1.9	071.2	18.0
AB8-8	37.55	Y	10	420-550	169.0	17.3	6.8	162.7	-50.9
AB8-9	40.33	Y	7	380-500	189.3	21.8	17.8	192.4	-47.4
AB8-9a	40.70	Y	6	490-540	161.9	-0.5	5.8	134.9	-63.0
AB8-10	41.84	Y	9	440-550	140.8	12.0	5.9	126.5	-39.1
AB8-11	45.83	Y	7	460-542	085.0	6.8	3.1	095.4	7.9
AB8-12	48.22	N	9	440-550	312.5	-37.7	2.2	322.8	16.5
AB8-12b	50.80	N	5	500-540	322.6	-47.1	4.1	335.1	14.5
AB8-14	54.02	Y	15	380-565	040.9	-18.4	3.8	049.1	35.2
AB8-14a	57.00	Y	7	470-540	296.7	-34.1	1.3	312.0	8.4
AB8-15	57.80	Y	11	400-550	154.5	19.3	2.0	145.9	-42.9
AB8-16	60.23	Y	11	460-565	231.5	-12.3	1.9	270.1	-41.1
AB8-18a	59.52	Y	7	470-540	260.1	-22.2	0.5	289.0	-17.1
AB8-16a	61.60	Y	7	470-540	245.4	-6.4	0.8	268.3	-26.2
AB8-17	63.34	Y	7	480-550	047.8	-12.0	4.8	060.2	33.9
AB8-17a	64.90	Y	7	470-540	344.5	-20.8	2.1	338.5	46.1
AB8-18	66.28	Y	8	440-550	144.6	10.8	5.0	128.5	-42.8
AB8-18b	66.88	Y	5	490-530	251.7	-20.8	8.1	285.5	-24.3
AB8-18c	67.14	Y	7	470-540	152.3	15.3	1.5	140.2	-44.8
AB8-18d	67.42	Y	10	400-540	143.1	13.5	4.3	129.9	-39.9
AB8-18j	68.99	N	3	500-530	311.0	-47.3	2.4	329.3	9.1
AB8-19	69.06	N	9	420-550	317.5	-44.2	8.2	330.4	14.5
AB8-20	69.18	N	7	440-535	323.6	-57.6	5.2	341.9	6.4
AB8-20a	69.48	N	4	500-530	315.0	-56.0	5.8	337.2	4.7
AB8-21	72.25	Y	12	480-565	017.6	-3.7	8.5	037.3	61.2
AB8-22	75.84	Y	6	440-528	000.1	-18.5	5.0	359.6	51.5
AB8-23	78.18	Y	7	520-560	304.1	12.3	5.6	269.8	35.0
AB8-24	81.36	N	10	440-560	325.7	-35.0	5.1	329.3	25.6
AB8-25	82.82	N	10	440-555	313.1	-33.1	8.4	319.6	19.9
AB8-26	83.70	N	11	500-565	325.5	-40.4	1.9	332.7	21.2
AB8-27	85.62	N	8	460-550	336.6	-47.3	11.0	343.7	19.2
AB8-28	88.09			Unstable magnetization above 480°C					
AB8-29	91.59	N	5	440-520	312.8	-44.6	3.5	328.2	11.9
AB8-30	94.62	N	2	450-550	322.2	-36.4	4.0	327.8	22.7
AB8-31	94.72	N	4	450-542	309.7	-25.2	8.5	311.1	22.7

AB8-32	97.94	Y	2	450-542	224.2	-7.8	4.5	261.0	-46.5
AB8-33	102.83	Y	11	420-560	005.5	-32.1	7.9	005.8	37.7
AB8-34	105.94	Y	5	520-550	208.4	1.3	10.3	235.8	-55.7
AB8-35	108.88	Y	14	380-550	278.9	-35.8	3.8	307.2	-5.5
AB8-36	111.91			Unstable magnetization above 480°C					
AB8-37	111.99	Y	7	380-520	29.7	-46.2	14.1	21.6	18.9
AB8-35a	114.39			Unstable magnetization above 425°C					
AB8-38	114.44			Unstable magnetization above 300°C					
AB8-39	119.05	Y	6	420-528	359.8	-29.5	4.8	359.6	40.5
AB8-39a	120.03	Y	7	450-530	019.0	-47.1	5.6	014.0	21.0
AB8-40	123.47			Unstable magnetization above 350°C					
AB8-41	124.78			Unstable magnetization above 350°C					
AB8-42	128.75			Unstable magnetization above 480°C					
AB8-42a	128.91	Y	8	425-530	227.9	-35.7	8.8		
AB8-42b	130.07			Unstable magnetization above 470°C					
AB8-44	132.10	Y	11	200-500	255.1	-36.8	8.1	303.4	-24.3
AB8-44a	133.83			Unstable magnetization above 450°C					
AB8-45	135.02			Unstable magnetization above 380°C					
AB8-46	136.99	N	9	380-535	305.0	-29.7	14.8	312.3	16.7
AB8-47a	140.95	N	4	450-500	306.8	-33.0	3.9	316.0	15.9
AB8-48	141.88	N	5	440-520	308.8	-31.7	5.9	316.0	18.1

ID: specimen number (bold: core segment with verified Ballmark orientation); *d*: down-core depth; Spun?: (Y)es/(N)o; *n*: number of steps in component fit; Temp.: temperature range of fit; *Dg*: geographic declination; *Ig*: geographic inclination; MAD: maximum angular deviation of PCA fit; *Ds*: Structurally corrected declination; *Is*: Structurally corrected inclination. Unstable magnetization indicates specimens with incoherent step-to-step magnetizations that yielded no distinct magnetic components. Data table is divided into sections of simultaneously retrieved segments of fractured core.

Table S2. Ebm plane fits

ID	<i>d</i> (m)	Spun?	<i>n</i>	Temp (°C)	<i>Dgp</i> (°)	<i>Igp</i> (°)	MAD (°)	<i>Dgcf</i> (°)	<i>Igcf</i> (°)	<i>Dscf</i> (°)	<i>Isf</i> (°)
AB8-13b	53.70	N	24	0-540	009.1	66.6	13.3	324.3	-17.1	314.3	38.3
AB8-18e*	67.70	N	13	335-540	074.3	-26.9	10.0	316.8	-42.3	328.6	15.6
AB8-18f*	67.81	N	19	150-540	114.4	-29.7	24.5	324.5	-56.6	341.7	7.5
AB8-18g*	68.34	N	19	100-540	341.5	45.2	18.7	314.9	-41.6	327.1	15.1
AB8-18h*	68.75	N	12	50-425	005.9	47.8	10.5	321.2	-32.8	324.6	24.9
AB8-18i*	68.87	N	12	50-540	329.9	53.3	22.5	316.1	-35.9	323.6	19.8
AB8-39b	122.08	N	6	470-530	061.4	11.0	12.5	340.5	-39.2	343.1	27.8
AB8-44	132.10	N	12	125-500	122.2	-41.4	20.1	316.7	-47.7	332.3	11.5
AB8-47	139.04	N	10	50-380	028.4	53.9	3.9	330.7	-21.3	323.7	39.2

ID: specimen number. *:great circle path is consistent with EBm mean direction from linear fits; *d*: down-core depth; Spun?: (Y)es/(N)o; *n*: number of steps in component fit; Temp.: temperature range of fit; *Dgp*: geographic declination of pole to great circle fit; *Igp*: geographic inclination of pole to great circle fit; MAD: maximum angular deviation of PCA fit; *Dgcf*: geographic declination of best fit line on great circle path; *Igcf*: geographic inclination of best fit line on great circle path; Structurally corrected declination; *Dscf*: *Dgcf* with structural correction applied; *Isf*: *Igcf* with structural correction applied.

Table S3. EBp component fits

ID	<i>d</i> (m)	Spun?	<i>n</i>	Temp (°C)	<i>Dg</i> (°)	<i>Ig</i> (°)	MAD (°)	<i>Dgc</i> (°)	<i>Igc</i> (°)
AB8-2	23.29	Y	8	200-420	8.1	-49.2	18.4	5.9	20.5
AB8-3	25.45	Y	7	250-440	175.5	-1.2	8.3	164.4	-70.4
AB8-4	26.53	Y	7	250-440	124.5	15.9	24.7	119.7	-23.9
AB8-5	29.46	Y	3	250-340	88.4	26.1	4.5	115.0	10.9
AB8-6	31.57	Y	5	200-380	69.9	16	17.3	99.9	24.8
AB8-7	34.34	Y	6	200-400	82.9	16.2	11.3	103.8	12.9
AB8-8	37.55	Y	6	300-440	183.5	-15.2	12.1	207.8	-84.6
AB8-9	40.33	Y	7	250-440	213.6	8	1.4	233.0	-47.4
AB8-11	45.83	Y	7	250-440	119.9	27.6	11.9	127.9	-14.1
AB8-12	48.22	N	7	250-440	345.3	-30.7	7.2	344.0	37.1
AB8-13a	51.62	Y	6	200-375	83.3	20.7	4.6	108.3	13.8
AB8-18a	59.52	Y	5	200-350	123.8	11.6	10.1	115.2	-25.5
AB8-19	69.06	N	6	200-400	347.3	-17.5	10.1	340.4	50.2
AB8-20	69.18	N	4	300-400	354.2	-19.4	5.8	351.0	50.0
AB8-21	72.25	Y	5	200-380	45.9	9.2	9.1	83.7	45.4
AB8-22	75.84	Y	5	200-400	22.7	-45.4	2.9	17.2	21.7
AB8-23	78.18	Y	7	200-420	351.9	-10.1	9.6	343.6	58.6
AB8-24	81.36	N	7	200-420	351.7	-22.9	6.8	348.6	46.2
AB8-25	82.82	N	7	200-420	343	-17	20.3	334.2	49.0
AB8-29	91.59	N	7	200-420	5.2	-13	16.1	8.5	56.7
AB8-30	94.62	N	5	250-450	350.7	-31.8	10.2	350.0	37.3
AB8-33	102.83	Y	5	250-450	31.7	-25.9	10.3	35.2	35.3
AB8-34	105.94	Y	5	250-450	241.8	-20.3	1.7	282.7	-33.3
AB8-35	108.88	Y	5	250-450	321.7	-28.9	5	322.0	28.1
AB8-36	111.91	Y	5	250-450	36.1	-24	8.7	40.5	34.3
AB8-37	111.99	Y	5	250-450	29.7	-27.7	11.7	32.2	34.8
AB8-38	114.44	Y	5	250-340	34.8	0.3	2.8	64.3	51.5
AB8-40	123.47	Y	4	300-380	315	-54.6	1.9	336.2	5.7
AB8-42	128.75	Y	4	250-400	259.5	-22.5	4.1	289.1	-17.7
AB8-44	132.1	Y	4	250-400	258.7	-39.5	6.6	306.7	-21.8
AB8-45	135.02	Y	5	300-400	9.2	-29.8	5.9	10.2	39.6
AB8-46	136.99	N	5	300-440	337.4	-13	11.5	324.0	49.6

ID: specimen number; *d*: down-core depth; Spun: (Y)es/(N)o; *n*: number of steps in component fit; Temp.: temperature range of fit; *Dg*: geographic declination; *Ig*: geographic inclination; MAD: maximum angular deviation of PCA fit; *Dgc*: Geographic declination corrected for sample misorientation; *Igc*: Geographic inclination corrected for sample misorientation.

Table S4. CDM component fits

ID	<i>d</i> (m)	Spun?	<i>n</i>	Temp (°C)	<i>Dg</i> (°)	<i>Ig</i> (°)	MAD (°)	<i>Dss</i> (°)	<i>Iss</i> (°)
AB8-69a*	191.79	Y?	9	335-510	051.1	37.6	1.6	118.2	9.2
AB8-69b*	192.45	N	5	425-500+	025.2	24.0	2.7	103.6	31.3
AB8-70	194.27			Unstable magnetization above 380°C					
AB8-71*	196.64	N	9	400-520+	029.2	40.2	2.5	121.6	26.1
AB8-71a*	197.86	N	4	470-520	22.5	30.5	11.3	111.5	33
AB8-72	199.83			Unstable magnetization above 400°C					
AB8-73	202.20	N	11	440-500+	027.3	23.9	2.7	103.4	29.4
AB8-73a	203.7	N	6	500-540	012.9	41.9	1.7	127.5	37.4

AB8-74	205.00	N	16	460-550	035.8	15.8	2.6	94.7	21.1
AB8-75	207.97	N	8	460-550	55.5	41.1	3.6	122.1	6.2
AB8-75a*	209.90	Y?	7	450-530	092.2	22.2	4.4	113.8	-29
AB8-76*	211.16	Y	8	460-520+	117.3	62.6	8.6	158.6	-14.4
AB8-77a	215.86	Y	9	425-540	054.9	57	3.7	138.0	8.4
AB8-78a	215.87	Y	14	325-540	127.0	2.1	2.9	114.0	-68.3
AB8-78b*	216.44	N	3	510-530+	350.3	14.4	14.8	94.4	65
AB8-80	220.16	Unstable magnetization above 340°C							
AB8-82	223.03	Unstable magnetization above 340°C							
AB8-84a*	226.73	Y	4	400-470+	230.0	35.8	5.6	225.3	1.6
AB8-84b*	227.98	Y	6	450-540	155.9	26.3	6.6	187.3	-52.4
AB8-85a*	230.96	Y	5	490-540	178.7	43.4	4.9	198.7	-28.6
AB8-86a*	234.84	Y	6	490-530	303.8	7.9	11.4	265	68.8
AB8-87	236.20	drilling overprint							
AB8-88	240.10	drilling overprint							
AB8-89*	244.10	N	7	400-520	353.1	1.7	5.0	66.8	61
AB8-90*	246.49	N	5	400-480	005.7	-17.1	5.7	47.8	41.7
AB8-91	248.86	Not origin trending before becoming unstable above 500C, GC path toward AB8-90							
AB8-92	252.73	N	10	500-565	022.4	-7.0	7.8	67.2	30.5
AB8-93	255.50	Unstable magnetization, possible hematite component?							
AB8-94,95,97		drilling overprint							
AB8-96*	262.17	N	5	528-555	021.7	-42.5	5.8	31.4	16.5
AB8-98	269.52	Y	9	528-575	222.5	12.2	4.1	247.0	-10.1
AB8-99	272.11	drilling overprint							
AB8-99a	272.99	drilling overprint							
AB8-99b*	273.06	N	7	490-540	021.3	-13.2	7.6	60.0	27.9
AB8-100	274.99	drilling overprint							
AB8-101	278.09	drilling overprint							
AB8-101a	278.75	drilling overprint							
AB8-102*	281.01	N	7	440-535	023.5	14.9	9.9	092.9	32.9
AB8-103	284.12	N	5	460-535	013.9	11.0	7.4	87.4	42.1
AB8-103a	284.88	drilling overprint							
AB8-106	289.89	drilling overprint							
AB8-107	292.97	Unstable magnetization above 440°C							
AB8-107a	293.96	Unstable magnetization above 340°C							
AB8-108*	295.60	N	6	460-535	018.6	-15.6	12.0	56.3	31.3
AB8-109*	298.23	N	5	460-528	005.6	-2.5	7.1	66.5	47.9
AB8-110*	301.82	N	5	380-460	023.9	5.8	4.0	82.2	31.7
AB8-111*	304.75	N	7	440-535	350.8	3.1	14.5	68.3	63.7
AB8-111b*	302.38	Unstable magnetization							
AB8-111c*	307.90	Y	6	350-470+	126.9	20.8	4.5	141.2	-54.5
AB8-112a*	308.00	Y	6	425-510+	148.2	15.1	2.5	178.4	-64.9
AB8-112d*	309.65	Y	6	450-520	93.2	42.8	2.0	133.7	-19.2
AB8-112e*	311.02	Unstable magnetization							
AB8-113a*	311.40	Y	10	400-520	100.7	38.2	4.4	133.5	-26.5
AB8-113b	312.20	Y	8	450-540	050.6	25.2	3.4	105.7	8.3
AB8-114a	312.50	Y	8	450-540	054.2	28.6	9.5	109.6	5.5
AB8-114b	313.80	Y	5	450-510	53.8	17.9	5.0	98.9	4.3
AB8-114c	314.00	Y	8	450-520	058.6	17.2	3.8	106.4	3.3
AB8-115	316.27	Y	9	400-535	031.3	10.1	5.0	088.1	25.0

AB8-115a	316.70	Y	6	450-540	039.9	8.2	9.2	87.2	16.3
AB8-115b*	318.69	Y	4	470-510	273.5	0.6	4.0	268.4	37.8
AB8-116	318.88	Y	7	400-520	290.9	-17	4.3	299.6	46.8
AB8-117	321.64	Y	9	250-500	317.2	-12.5	6.8	331.8	66.3
AB8-117a	322.67	Y	7	425-540	060.3	30.4	5.2	112.2	0.6
AB8-118a*	324.10	N	6	400-510	021.3	-2.3	3.6	72.2	32.8
AB8-118*	324.09	N	8	400-535	353.0	-12.2	5.1	043.5	54.6
AB8-118b*	326.68	N	6	450-520	030.2	10.0	4.4	087.8	26.0
AB8-119	329.32	Y	6	400-500	131.6	40.9	3.7	158.5	-37.7

ID: specimen number (*: magnetization direction is a linear fit forced through the origin); *d*: down-core depth; Spun?: (Y)es/(N)o; *n*: number of steps in component fit; Temp.: temperature range of fit; *Dg*: geographic declination; *Ig*: geographic inclination; MAD: maximum angular deviation of PCA fit; *Dss*: Declination structurally corrected for the dip of the Euro Basalt and then the remaining dip of the Double Bar-Coucal section; *Iss*: Inclination structurally corrected for the dip of the Euro Basalt and then the remaining dip of the Double Bar-Coucal section. "Unstable magnetization" indicates specimens with incoherent step-to-step magnetizations that yielded no distinct magnetic components. Drilling overprint indicates specimens that retained a strong DOP component to high temperatures.

Table S5. CDp component fits

ID	<i>d</i> (m)	Spun?	<i>n</i>	Temp. (°C)	<i>Dg</i> (°)	<i>Ig</i> (°)	MAD (°)	<i>Dss</i> (°)	<i>Iss</i> (°)
AB8-61	170.10	Y	3	200-380	078.9	-7.1	5.9	078.1	-24.5
AB8-63	172.33	Y	5	150-380	073.1	44.6	1.8	128.6	-5.5
AB8-64	176.52	Y	4	200-380	055.6	8.6	9.4	090.0	1.0
AB8-65	179.36	Y	3	250-380	093.2	9.1	5.5	099.9	-34.9
AB8-66	182.32	Y	4	200-380	092.1	16.6	32.9	107.8	-31.2
AB8-67	185.43	Y	4	200-380	080.2	-41	11.6	040.6	-25.3
AB8-68	187.93	Y	4	200-380	081.0	-26.2	13	056.9	-27.5
AB8-69	191.32	Y	4	200-380	049.8	-4.6	17	076.0	4.5
AB8-69a	191.79	Y	5	200-380	052.0	9.5	13.4	090.3	4.7
AB8-70	194.27	Y	4	200-380	088.1	29.3	4.6	119.0	-22.5
AB8-71	196.64	N	4	200-380	035.6	1.0	2.0	079.0	19.4
AB8-72	199.83	Y	4	200-380	107.6	31.8	9.4	132.2	-35.0
AB8-73	202.20	N	5	200-380	006.0	-13.2	4.9	052.6	43.3
AB8-75a	209.90	Y	6	150-340	085.2	-8.0	7.9	078.0	-30.8
AB8-76	211.16	Y	6	150-340	115.4	55.7	5.8	154.1	-19.9
AB8-77	213.82	Y	4	200-380	070.9	25.2	1.1	109.4	-9.7
AB8-78	216.43	Y	6	100-340	064.8	13.3	1.0	096.3	-7.0
AB8-84	226.08	Y	9	50-340	011.1	11.3	3.2	087.6	44.9
AB8-85	229.58	Y	5	0-400	184.5	33.8	2.0	210.1	-32.5
AB8-86	233.61	Y	10	0-300	174.2	42	1.4	196.5	-31.7
AB8-89	244.10	Y	5	150-340	358.8	-18.3	7	041.2	46.5
AB8-90	246.49	Y	3	250-380	016.7	-31.7	1.2	039.0	25.5
AB8-102	281.01	N	3	250-380	345.4	-12.3	7.5	034.1	60.1
AB8-103	284.12	N	4	250-340	010.9	2.8	2.6	075.7	44.0
AB8-104	287.00	Y	8	125-340	003.6	-21.5	1.5	041.4	40.9
AB8-107	292.97	Y	3	250-380	353.0	-42.4	1.5	015.4	31.9
AB8-109	298.23	N	3	250-380	017.3	-8.7	10.3	063.5	34.9

AB8-111	304.75	N	4	250-340	357.9	-14.3	6.4	045.3	49.5
AB8-111a	302.20	Y	6	280-375	179.6	53.5	11.2	192.4	-20.2
AB8-116	318.88	Y	5	280-340	314.0	-7.2	4.3	318.0	69.6
AB8-118	324.09	N	5	280-340	345.3	-30.3	6.6	016.5	45.4
AB8-119	329.32	Y	5	280-340	128.6	31.1	10.0	150.8	-46.1

ID: specimen number; *d*: down-core depth; Spun?: (Y)es/(N)o, based on interpretation of CDm component from each specimen; *n*: number of steps in component fit; Temp.: temperature range of fit; *Dg*: geographic declination; *Ig*: geographic inclination; MAD: maximum angular deviation of PCA fit; *Dss*: Declination structurally corrected for the dip of the Euro Basalt and then the remaining dip of the Double Bar-Coucal section; *Iss*: Inclination structurally corrected for the dip of the Euro Basalt and then the remaining dip of the Double Bar-Coucal section.

Table S6. Zircon geochronology references

ID	Sample Number	Unit	Age (Ma)	Method	Detrital?	Reference
1	GSWA 142836	Strelley Pool Fm.	3426±10	SHRIMP	Yes	(Nelson, 1998)
2	GSWA 142972	Strelley Pool Fm.	3433±6	SHRIMP	Yes	(Nelson, 2001)
3	GSWA 168913	Strelley Pool Fm.	3427±2	SHRIMP	No	(Nelson, 2001)
4	MP1	Strelley Pool Fm.	3430	SHRIMP	Yes	(Barley et al., 1998)
5	GSWA 160221	Panorama Fm.	3430±4	SHRIMP	No	(Nelson, 2002)
6	GSWA 148502	Panorama Fm.	3433±2	SHRIMP	Maybe	(Nelson, 2001)
7	JW95-001	Panorama Fm.	3446±5	SHRIMP	No	(de Vries et al., 2006)
8	100507	Panorama Fm.	3458±2	TIMS	No	(Thorpe et al., 1992)
9	MW19	Footbridge Ch.	3334±3	1 grain TIMS	No	(Byerly et al., 1996)
10	GSWA 178042	Euro Basalt	3350±5	SHRIMP	Maybe	(Nelson, 2005)
11	–	Hooggenoeg H6	3445±4	TIMS	No	(de Wit et al., 1987)
12	MW64	Kromberg Fm.	3416±5	TIMS	Maybe	(Kröner et al., 1991)
13.1	BA 10	Noisy Complex	3438±6	TIMS	Yes	(Kröner and Todt, 1988)
13.2	BA 11	Noisy Complex	3438±6	TIMS	Yes	(Kröner and Todt, 1988)
14.1	KD2-116m	Noisy Complex	~3437	LA-ICPMS	Yes	(Grosch et al., 2011)
14.2	KD2-176m	Noisy Complex	~3436	LA-ICPMS	Yes	(Grosch et al., 2011)
15	GSWA 144681	Wyman Fm.	3315±5	SHRIMP	No	(Nelson, 2002)
16	94754	Wyman Fm.	3325±2	TIMS	No	(Thorpe et al., 1992)
17	GSWA 169026	Panorama Fm?	3458±9	SHRIMP	Yes	(Nelson, 2004)
18	–	Hooggenoeg	3451±5	SHRIMP	No	(De Vries, 2004)
19	94003	Wyman Fm.	3315±3	SHRIMP	No	(Buick et al., 2002)

Table S7. Selected virtual geomagnetic poles (VPGs) from the East Pilbara and Kaapvaal cratons

ID	Ref	Age (Ma)	λ_g (°)	Φ_g (°)	dp_g (°)	dm_g (°)	λ_s (°)	Φ_s (°)	dp_s (°)	dm_s (°)
EBm	A	~3350	49.6	17.7	3.8	6.3	46.5	68.3	2.8	5.4
CDm	A	>3350	60.0	154.4	5.3	10.5	-2.3	186.4	7.4	12.4
DFM1	B	3464-3471	-17.5	38.4	6.8	12.5	46.4	84.8	6.9	12.6

DFM2	B	3464-3471	73.5	49.1	8.3	15.2	42.3	87	9.3	16.1
DFH	B	?	-17.5	4.2	8.9	16.2	-17	61.5	14.6	20.6
DFL	B	<3465	55.7	131.4	7.1	13.3	-28	349.3	8.7	14.7
MBL	C	<3458	-31.8	248.8	12.9	22.7	–	–	–	–
MB-1	C	3458-3471	58.5	145.9	6.3	A95	67.4	358.2	6.3	A95
Apex	D	~3458	22.4	72.3	12.6	20	38.2	19.4	10.8	18.5
MDS	E	755±3	43.8	134.1	5.1	5.1	–	–	–	–
KOM	F	3472-3482	–	–	–	–	50.0	66.9	7.9	15.5
HT2	G	3472-3455	12.0	57.0	18.9	24.0	63.4	70.3	12.7	25.1
NfT	G	3455	-43.7	193.8	3.1	5.5	-36.8	216.9	4.4	6.9
NfD-U	G	3455	-13.3	232.8	25	39.6	59.5	32.5	16	31.8
P0	H	>2772	–	–	–	–	-1.5	93.6	8.2	A95
P1	H	~2772	–	–	–	–	-40.8	159.8	3.7	A95
P2	H	~2766	–	–	–	–	-46.5	152.7	15.2	A95
P4-7	H	2752-2721	–	–	–	–	-50.4	138.2	12.5	A95
P8-10	H	2718-2715	–	–	–	–	-59.1	186.3	6.1	A95
MT7-10	H	<2715, >1700	–	–	–	–	-53.2	203.9	5.3	A95
RB	I	~2772	–	–	–	–	-52.4	178.0	6.4	9.1
HP2	J	~1700	–	–	–	–	-35.3	211.9	3	A95
TPA	K	~1700	–	–	–	–	-37.4	220.3	5.7	11.3
NP	L	~3200	–	–	–	–	17.6	309.8	9	A95
KV+	M	~3200	–	–	–	–	-23.4	90.2	11.4	15.8
KV- (R)	M	~3200	–	–	–	–	8.4	291.1	5.1	9.6
DAL	M	~3200	–	–	–	–	-13.2	73.2	4.8	5.9
DER(K1)	N	2782±5	–	–	–	–	-39.6	4.7	17.5	A95
ALL	O	~2700	–	–	–	–	-65.5	339.5	6.5	A95

Table S7. References: A – this study, B – McElhinny and Senanayake (1980), C – Saganuma et al. (2006), D – Yoshihara (2001), E – Wingate and Giddings (2000); F – Hale and Dunlop (1984); G – Biggin et al. (2011); H – Strik et al. (2003); I – Schmidt and Embleton (1985); J – Li et al. (2000) ; K – Schmidt and Clark (1994); L – Layer et al. (1998); M – Tarduno et al. (2007); N – Wingate (1998); O – de Kock et al. (2009)

λ : latitude of VGP; Φ : longitude of VGP; dp , dm : semiminor and semimajor axes of 95% polar error ellipse; A95: error reported as Fisher 95% confidence interval; g subscript denotes geographic coordinates, s subscript denotes tilt-corrected data. Boldface: preferred interpretation of pole.

Figure S1. Backscattered electron micrographs of Double Bar Formation specimens collected from the alteration zone underlying the Strelley Pool Formation. Trellis structures from <0.1 to 2 mm in diameter are composed of leucoxene (TiO_2), interpreted as the remnants of [111] ilmenite exsolution lamellae of oxyexsolved igneous titanomagnetite. Spaces between trellis structures are filled with quartz, chlorite, and phengite. Highly reflective (white) areas are pyrite and arsenopyrite. The white bar in each image is a 200 μm scale bar.

Figure S2. Published binned mean directions from the Marble Bar Chert (Saganuma et al., 2006) in geographic coordinates. That these directions can be precisely fit by a small circle with a pole fixed to the drill core direction indicates that down-core directional variation is best explained by

progressive misorientation of the drill core with depth instead of by fast plate motion with respect to the stationary geomagnetic dipole field.

Figure S3. ABDP-8 core continuity log. The distribution of core sticks is indicated by alternating colored bands. The declination of ChRM for each of our subsamples (horizontal positions of small boxes) provides a simple proxy for the relative spin of specimens. Fragmented core (hatched areas) and observed breaks in core continuity (red lines) coincide with highly scattered declinations, while continuous sections of core with few breaks in continuity yield consistent declinations. Red squares are ChRM directions included in paleomagnetic means. Circled specimens were collected from core segments bearing the direct Ballmark orientation line (not propagated from another segment).

Figure S4. The effects of core misorientation on ChRM directions and bedding poles from Coucal Formation specimens. Specimens are from a highly fragmented portion of the core, but are collected from core segments bearing a fiducial line. The best-fit small circle to bedding poles is consistent with the bedding pole observed at the surface, supporting our interpretation of core azimuthal misorientation. The best-fit small circle to ChRM directions is also consistent with core azimuthal misorientation. Back-rotation of samples specimens to match the surface bedding orientation would yield northward trending, shallowly plunging ChRM directions dissimilar from the EBm component but similar to the CDm directions for confidently oriented core samples.

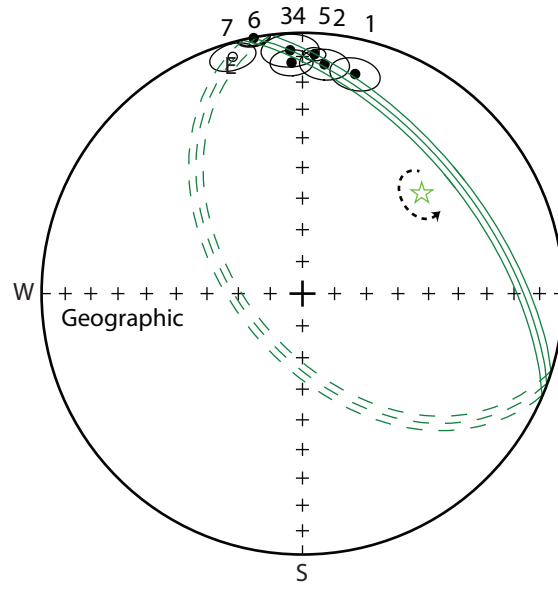


Figure S2.

